Journal of Colloid and Interface Science 584 (2021) 669–683

Contents lists available at ScienceDirect

Journal of Colloid and Interface Science

journal homepage: www.elsevier.com/locate/jcis

Regular Article

Polyelectrolyte complex templated synthesis of monodisperse, sub-100 nm porous silica nanoparticles for cancer targeted and stimuli-responsive drug delivery

George Newham[a], Ryan K. Mathew[b,c], Heiko Wurdak[a], Stephen D. Evans[a], Zhan Yuin Ong[a,b,*]

[a] School of Physics and Astronomy, University of Leeds, Leeds LS2 9JT, UK
[b] Leeds Institute of Medical Research at St. James's, School of Medicine, University of Leeds, Leeds LS2 9JT, UK
[c] Department of Neurosurgery, Leeds General Infirmary, Leeds Teaching Hospitals NHS Trust, UK

GRAPHICAL ABSTRACT

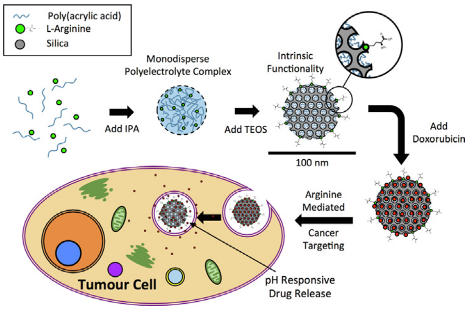

ARTICLE INFO

Article history:
Received 8 August 2020
Revised 30 September 2020
Accepted 28 October 2020
Available online 3 November 2020

Keywords:
Porous silica nanoparticle
Polyelectrolyte complex
Cancer targeting
Drug delivery
Glioblastoma

ABSTRACT

Porous silica nanoparticles (PSiNPs) have long attracted interest in drug delivery research. However, conventional synthesis methods for sub-100 nm, functionalised PSiNPs typically give poor monodispersity, reproducibility, or involve complex synthetic protocols. We report a facile, reproducible, and cost-effective one-pot method for the synthesis of cancer targeting and pH responsive PSiNPs in this size range, without the need for post-synthetic modification. This was achieved by using monodisperse L-arginine (Arg)/ poly(acrylic acid) (PAA) polyelectrolyte complexes (PECs) as soft templates for silane hydrolysis and condensation. Highly uniform PSiNPs with tunable size control between 42 and 178 nm and disordered pore structure (1.1–2.7 nm) were obtained. Both PAA and Arg were retained within the PSiNPs, which enabled a high doxorubicin hydrochloride (Dox) loading capacity (22% w/w) and a 4-fold increase in drug release under weakly acidic pH compared to physiological pH. The surface presentation of Arg conferred significantly higher intracellular accumulation of Arg/PAA-PSiNPs in patient-derived glioblastoma cells compared to non-tumorigenic neural progenitor cells, which effectively translated to lower IC50 values for Dox-loaded Arg/PAA-PSiNPs than non-functionalised PSiNPs.

Abbreviations: PSiNP, Porous Silica Nanoparticle; Arg, L-Arginine; PAA, Poly(acrylic Acid); FITC, Fluorescein isothiocyanate; PBS, Phosphate Buffered Saline; PEC, Polyelectrolyte Complex; TEOS, Tetraethoxysilane; TEM, Transmission Electron Microscopy; WST-1, (4-[3-(4-Iodophenyl)-2-(4-nitro-phenyl)-2H-5-tetrazolio]-1,3-benzene disulfonate); BCA, Bicinchoninic acid; DLS, Dynamic Light Scattering; bFGF, Basic Fibroblast Growth Factor; rhEGF, Recombinant Human Epidermal Growth Factor; IPA, 2-propanol; Dox, Doxorubicin Hydrochloride; IC_{50}, Half Maximal Inhibitory Concentration; ATR FTIR, Attentuated Total Reflection Fourier Transform Infrared Spectroscopy; TGA, Thermogravimetric Analysis; BET, Brunauer–Emmett–Teller; NLDF, Non-Local Density Functional Theory; CAT-1, Cationic Amino Acid Transporter 1; HSNP, Hollow Silica Nanoparticle; CTAB, Cetrimonium Bromide; ASS, Argininosuccinate Synthetase; PDI, Polydispersity Index.

[*] Corresponding author.
E-mail address: z.y.ong@leeds.ac.uk (Z.Y. Ong).

https://doi.org/10.1016/j.jcis.2020.10.133
0021-9797/© 2020 The Authors. Published by Elsevier Inc.
This is an open access article under the CC BY license (http://creativecommons.org/licenses/by/4.0/).

This work brings forward new insights for the development of monodisperse PSiNPs with highly desirable built-in functionalities for biomedical applications.

© 2020 The Authors. Published by Elsevier Inc. This is an open access article under the CC BY license (http://creativecommons.org/licenses/by/4.0/).

---

1. Introduction

Porous silica nanoparticles (PSiNPs) are amongst the most promising vehicles for drug delivery. Made of chemically inert silica, their biocompatibility, large internal pore volumes, high surface areas, and ease of functionalisation, have long attracted attention in medical research [1]. Their enhanced degradation by the increased reactive oxygen species (ROS) levels observed in the tumour microenvironment further supports their suitability for chemotherapeutic delivery as shown by the recent approval of silica-based ‘C dots’ for Phase 2 clinical trials [2,3].

PSiNPs are most commonly synthesised through a modified Stöber method, a sol–gel process using the surfactant, cetrimonium bromide (CTAB), as a template for the porous structure. Particle size and morphological control is achieved though varying reagent concentrations, reaction temperature, and pH. However, this method does not typically allow the synthesis of highly uniform sub-100 nm particles, which are optimal for prolonged blood circulation, tumour accumulation, and enhanced cell uptake [4,5]. Adaptations of this method have been used to access the sub-100 nm range, but they often lead to poor monodispersity, poor reproducibility, or require complex synthetic protocols [6–8]. In addition, all of these protocols require additional calcination or chemical extraction steps to remove the templating surfactant to access the porous structures, modify the chemical properties of the final products, and possibly reduce toxicity before biological application.

To achieve efficient drug delivery, there is a strong impetus for the chemical functionalisation of PSiNPs with cancer targeting ligands and/or stimuli-responsive moieties for controlled or triggered drug release [9]. However, the current preparation of functionalised PSiNPs typically involves lengthy post-synthetic modifications with multiple synthesis, purification, and characterisation steps, significantly increasing the time and cost of synthesis. This in turn greatly decreases the likelihood of their successful translation into industrial and clinical use. Therefore, there remains a crucial need for a facile, reproducible, and cost-effective synthetic method to obtain monodisperse sub-100 nm PSiNPs with intrinsic cancer targeting and stimuli-responsive drug release properties without the requirement for further post-synthetic modifications.

The polyelectrolyte complex (PEC) templated synthesis method has emerged as a promising strategy for the facile preparation of various types of nanoparticles suitable for drug delivery or biological imaging such as PSiNPs [10,11], $CaCO_3$ [12,13], zeolitic imidazolate framework-8 [14], and lanthanide-doped gadolinium oxide nanoparticles [15]. The mixing of oppositely charged polymers or charged polymers with small counterions forms PECs whose size, polydispersity, surface properties, and chemical functionality may be precisely tuned. PECs formed from poly(acrylic acid) (PAA) and NH_4^+ in mixed water–ethanol solvents have been extensively used as templates to give hollow silica nanoparticles (HSNPs) [16–19]. This method, however, typically leads to large particle sizes or poor polydispersity. Recently, the superior ability of divalent cations to crosslink PAA chains and form small, monodisperse PECs was demonstrated. The use of Mg^{2+} and Ca^{2+} to complex with PAA in hollow silica particle synthesis gave both smaller particle sizes and narrower size distributions compared to monovalent cations NH_4^+, K^+, and Na^+ [20]. However, the PAA templates within the synthesised HSNPs were easily removed by rinsing with water during purification, resulting in the loss of potential functionality. In contrast, the use of polyvalent poly(L-glutamic acid) with poly(2-(*N*,*N*-diethylamino) ethylmethacrylate) was found to give more stable PEC templates that were retained after PSiNP synthesis and purification [10]. The hybrid PSiNPs were shown to permit doxorubicin (Dox) loading and confer pH responsive drug release. Similarly, the post-synthetic retention of PAA within $CaCO_3$ and zeolitic imidazolate framework-8 nanoparticles templated from PAA/Ca^{2+} and PAA/Zn^{2+}, respectively [13,14] has also afforded a high drug loading capacity and a pH responsive drug release kinetic. However, for these systems, electron microscope imaging showed that the size distributions of the synthesised nanoparticles remained broad. There is thus a need to further explore and tailor the use of other PEC combinations to improve the uniformity and retain the PEC constituents within the nanoparticles to provide desirable functionalities for biomedical applications in a facile and cost-effective manner.

In this study, we report a novel one-pot synthesis method to obtain monodisperse, sub-100 nm PSiNPs with intrinsic cancer targeting, efficient drug loading, and pH responsive drug release behaviour by exploiting the unique alcohol induced polyelectrolyte complexation of L-arginine (Arg) and PAA (Scheme 1). The efficacy of Arg in the formation of PECs and its ability to template the synthesis of PSiNPs is further compared to a second cation, NH_4^+. The key motivations behind the choice of Arg and PAA in the PEC template are as follows: (1) Cationic Arg is expected to undergo strong electrostatic interactions with anionic PAA to form highly uniform, colloidally stable PECs, and act as a basic catalyst for silane mineralisation on the Arg/PAA PEC network to yield PSiNPs with high porosity and surface areas. (2) The retention of both PAA and Arg within the PSiNPs facilitates efficient anticancer drug loading through enhanced electrostatic interactions, as well as promoting acidic pH responsive drug release. (3) Surface presentation of Arg on the PSiNPs is expected to confer excellent colloidal stability and cancer targeting capabilities. Due to argininosuccinate synthetase (ASS) deficiencies in many solid cancers such as glioblastoma multiforme (GBM), melanoma, and prostate, auxotrophic tumour cells greatly rely on exogenous Arg to sustain their development and progression [21–23]. The Arg transporter, cationic amino acid transporter-1 (CAT-1), has been found to be overexpressed in many malignancies to enhance Arg uptake and accumulation in tumour cells [24]. There is thus significant potential to improve the delivery of anticancer therapeutics to tumour cells *via* Arg functionalisation of nanocarriers. Indeed, Wang *et al.* recently demonstrated efficient delivery of Mn^{2+} and Dox using Arg-capped manganese silicate nanobubbles to give significant tumour suppression in a Huh7 xenograft nude mice model [25]. Despite the promising results, this cancer targeting strategy remains poorly exploited in nanoparticle mediated drug delivery systems. Herein, we demonstrate excellent control over the size and dispersity of Arg/PAA PECs and resulting PSiNPs by varying the concentration of isopropanol, polyelectrolytes, and silanes. The relationship of the silane volume to PEC template size and its effect on particle diameter and monodispersity was comprehensively explored. This relationship was further used to modulate the surface presentation of Arg and hence the efficacy of cancer

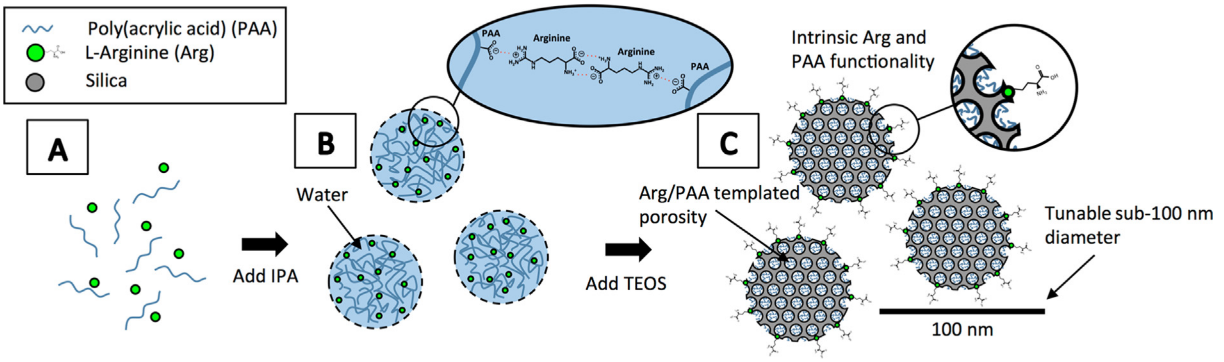

Scheme 1. A schematic showing the polyelectrolyte templated synthesis of Arg/PAA-PSiNPs. (A) PAA and Arg are initially dissolved in water, and (B) upon addition of 2-propanol (IPA), the electrostatically associated PAA and Arg assemble into aqueous PECs in bulk IPA. (C) The PECs act as templates for the hydrolysis and condensation of the silica precursor triethoxysilane (TEOS) to form hybrid Arg/PAA-PSiNPs with intrinsic PAA and amino acid functionality.

targeting for the first time with PEC templated PSiNPs. The cancer targeting capabilities and biosafety of the hybrid PSiNPs were successfully demonstrated in primary patient-derived GBM cells and non-tumorigenic neural progenitor cells. This study provides important insights for the reproducible, scalable, and cost-effective synthesis of monodisperse, multifunctional PSiNPs through the judicious choice of polyelectrolyte templates to achieve cancer targeting and pH-responsive drug delivery to improve anti-cancer efficacy.

2. Experimental section

2.1 Materials

L-arginine and ammonium hydroxide (28–30 wt% NH_3 solution in water) were purchased from Acros Organics. 2-Propanol (IPA; ≥ 99.7%) was purchased from VWR. Poly(acrylic acid) (PAA; M_w = 1800), 4-[3-(4-Iodophenyl)-2-(4-nitro-phenyl)-2H-5-tetrazolio]-1,3-benzene disulfonate (WST-1) reagent, and poly-L-ornithine were purchased from Sigma-Aldrich. Tetraethoxysilane (TEOS; 99.9%) was purchased from Alfa Aesar. Fluorescein isothiocyanate-poly(ethylene glycol) silane (FITC-PEG-silane; M_w = 5000) was obtained from Nanocs. Pierce BCA Protein Assay kit, DMEM/F-12 medium with GlutaMAX, neurobasal medium, B-27 supplement, N2 supplement, and mouse laminin protein were purchased form Thermo Fisher Scientific. Spectra/Por 7 regenerated cellulose dialysis tubing (1 kDa MWCO) was purchased from Spectrum Chemical. Recombinant human epidermal growth factors (rhEGF) and basic fibroblast growth factors (bFGF) were purchased from Bio Techne and doxorubicin HCl (Dox; 95%) was purchased from Fluorochem Limited. All chemicals were of analytical grade and used without further purification. Ultrapure water (Millipore Milli-Q) with 18.2 MΩ cm resistivity at 25 °C was used in all experiments.

2.2 Preparation of polyelectrolyte templates

To study the IPA-induced formation of Arg/PAA PECs, 100 μL of 1.1×10^1 mM PAA and 295 μL of 8.6×10^2 mM Arg were first added to 1605 μL of ultrapure water (2.0 mL final volume). The solution was dispersed in an ultrasonic bath for 5 min before the addition of IPA under stirring. The final volume was topped up to 10.0 mL with ultrapure water and left to stir for 1 h at room temperature. To form NH_4OH/PAA PECs, the same procedure was followed but with an equimolar amount of NH_4OH used in place of Arg. The final pH was 9.0 for both Arg/PAA and NH_4OH/PAA PECs. For the synthesis of PEC templates with varying amounts of PAA, Arg or NH_4OH, the total volume of the aqueous reagents was maintained at 2.0 mL and 8.0 mL of IPA was added under stirring.

2.3 Synthesis of Arg/PAA-PSiNPs and NH_4OH/PAA-PSiNPs

For the PSiNP syntheses presented herein, PEC templates were prepared with 100 μL of 1.1×10^1 mM PAA and 295 μL of 8.6×10^2 mM Arg (or 295 μL of 8.6×10^2 mM NH_4OH) in 80% v/v IPA (10 mL final volume). Subsequently, 20–500 μL of TEOS was added and the mixture was stirred at room temperature for 24 h. The final product was collected by centrifugation (17,000*g* for 1 h) and purified by rinsing thrice with ultrapure water. The reaction was also scaled up to 250 mL by increasing the volume of each reagent used by 25-fold using the same synthetic protocol. FITC-labelled PSiNPs were synthesised by the addition of ~ 0.1 mol % of FITC-PEG-silane and 1000 μL of TEOS to 250 mL final volume of the PEC templates in 80% v/v IPA.

2.4 Characterisation of PECs and PSiNPs

The hydrodynamic diameters and zeta-potentials of the PECs and PSiNPs were determined by dynamic light scattering (DLS) using the Zetasizer Nano equipped with a He-Ne laser and with scattered light detected at 173° (Malvern Instrument Ltd., Worcestershire, UK). Each sample was run thrice with 12 measurements per run at 25 °C and the size and zeta-potential measurements are reported as the mean ± standard deviation of the three runs. The morphology of the PSiNPs was characterised using high resolution TEM (FEI Tecnai G2-Spirit) operated at 120 kV accelerating voltage with a Gatan Ultrascan 4000 CCD camera. Typically, 5 μL of each sample was pipetted onto a carbon coated copper grid and allowed to dry at room temperature before imaging. The particle size distribution was determined from the obtained TEM images using the ImageJ analysis software. The FITC-labelled PSiNPs were characterised using UV–vis spectroscopy (Agilent Cary 5000) and fluorescence spectroscopy (Edinburgh Instruments F980) where 1 mL of sample was analysed in a quartz cuvette with 10 mm path length. In the collection of the fluorescence spectra, 0.1 mg/mL of FITC-labelled PSiNPs was excited at 488 nm and the emission counts were accumulated over 3 repeat measurements recorded between 375 and 650 nm at intervals of 0.5 nm with 1 s dwell time. To analyse the organic content of the PSiNPs, thermogravimetic analysis (TGA) was performed (Mettler Toledo TGA/DSC1 Star System). Prior to analysis, the PSiNPs were lyophilised and approximately 20 mg of sample was added to a crucible of known mass for analysis. Measurements were performed between 30 and 650 °C at a heating rate of 10 °C min^{-1} under nitrogen flow. PAA and Arg were used to obtain reference spectra.

The ATR-FTIR spectra were collected using the Thermo Scientific Nicolet iS10 equipped with the Thermo Scientific Smart iTX ATR sampling accessory. Spectral data was collected between 650 and 4000 cm^{-1} with a spectral resolution of 2 cm^{-1}. Nitrogen gas adsorption–desorption isotherms were recorded using the Micromeritics Tristar 3000 at 77 K with a 10 s equilibration interval. Before measurement, the samples were freeze-dried and degassed under vacuum at 100 °C for 4 h. The specific surface area of the sample was found using the Brunauer–Emmett–Teller (BET) plot as described by Roquerol *et al.* in the relative pressure range of 0.02–0.16 [26]. The pore size distribution was determined by non-local density functional theory (NLDFT) analysis of the adsorption data in the relative pressure range of 0–0.9 using the Micromeritics Microactive analysis software.

2.5 Drug loading and release

2 mg of Arg/PAA-PSiNPs or NH_4OH/PAA-PSiNPs were suspended in 1, 2, or 4 mg mL^{-1} of Dox solution (1.0 mL). The mixture was stirred at room temperature under dark conditions for 48 h. The Dox-loaded particles were collected by centrifugation (17,000*g* for 10 min) and rinsed thrice with ultrapure water to remove excess drug. To determine the drug loading capacity, the amount of non-encapsulated drug remaining in the supernatants from each rinse was determined by UV–vis spectroscopy at 480 nm using a standard calibration curve prepared from solutions of known Dox concentrations. The total amount of non-encapsulated drug in the supernatants was subtracted from the initial amount of drug added to determine the mass of drug loaded into the particles. The drug loading capacity was calculated using the following formula:

$$\text{Drug loading capacity (\%)} = (\text{Massofloadeddrug})/(\text{Massofparticles}) \times 100\% \tag{1}$$

To quantify the drug release rate, 9 mg of dox-loaded Arg/PAA-PSiNPs or NH_4OH/PAA-PSiNPs were suspended in 2.0 mL of water and transferred to a dialysis bag (1 kDa MWCO). The samples were dialysed against 50 mL of 1 × PBS (pH 7.4) or 239 mM sodium acetate buffer (pH 5.0) with equivalent ionic strengths at 37 °C under magnetic stirring. At regular time points, 1.0 mL of the dialysate was removed for analysis of Dox concentration and replaced with fresh buffer. The amount of drug released was quantified using UV–vis spectroscopy at 480 nm. The drug release kinetics and mechanisms were evaluated using the Korsmeyer-Peppas model [27]:

$$F = k_m t^n \tag{2}$$

Where F is the fraction of drug released, k_m is the kinetic constant dependent on the structural and geometric properties of the particles, and n is the release exponent which indicates the drug release mechanism. Data points up to 60% of drug release in the cumulative release curves were plotted on logarithmic scales, and the release exponent, n, was found from the gradient. The value for n was then substituted into Eq. (2) to find the kinetic constant, k_m.

2.6 Cell culture

Patient-derived glioblastoma GBM1 and GBM20 cells, which have been confirmed to retain the histopathological features of their parent tumours [28,29], were cultured on poly-L-ornithine and laminin-coated cell culture flasks in neurobasal medium supplemented with 0.5 × B-27, 0.5 × N-2, 40 ng/mL bFGF, and 40 ng/mL rhEGF. The non-tumourigenic adult brain neural progenitor NP1 cells were cultured in DMEM/F-12 medium supplemented with 0.5 × B-27, 0.5 × N-2, 20 ng/mL bFGF, and 20 ng/mL rhEGF, 1 × GlutaMax-1, and 5% fetal bovine serum. All cells were maintained at 37 °C with 5% CO_2.

2.7 Cytotoxicity testing

The cytotoxicity of the empty and Dox-loaded Arg/PAA-PSiNPs and NH_4OH/PAA-PSiNPs was determined using the WST-1 assay. GBM1, GBM20, and NP1 cells were seeded at a density of 8 × 10^3 cells per well in 96-well plates and left to adhere for 24 h. The cell culture media was replaced with fresh media containing 5–750 μg mL^{-1} of PSiNPs or Dox-loaded PSiNPs containing 0.01–50 μM of Dox and incubated for 24 h. After incubation, the cells in each well were rinsed with PBS, and 100 μL of fresh media containing 10 μL of WST-1 reagent was added to each well. The cells were then incubated for 2 h at 37 °C before the absorbance was determined at 440 nm using a microplate spectrophotometer (Molecular Devices SpectraMax M2e). Blank wells containing cell culture media and WST-1 (without cells) were included to determine the background absorbance. The cell viability of treated cells was determined by comparison to untreated controls as follows:

$$\text{Cell viability (\%)} = [(A_{\text{Treated}} - A_{\text{Background}})/(A_{\text{UntreatedControl}} - A_{\text{Background}})] \times 100\% \tag{3}$$

2.8 Cellular uptake studies

GBM1, GBM20, and NP1 cells were seeded at a density of 8 × 10^3 cells per well in 96-well plates and allowed to adhere for 24 h. The cells were incubated with fresh media containing 200 μg mL^{-1} FITC-labelled Arg/PAA-PSiNPs and NH_4OH/PAA-PSiNPs for 4 h before carefully rinsing the cells 5 times with PBS to remove non-internalised PSiNPs. The cells were lysed with 1% v/v triton-X100 in PBS and the fluorescence intensity of the lysate was determined at 420 nm excitation and 518 nm emission wavelengths with a microplate spectrophotometer. To determine the concentration of PSiNPs taken up by the cells, the measured fluorescence intensity was compared to a calibration curve prepared from known FITC-labelled PSiNP concentrations in the same 1% v/v triton-X100 solution. The protein content of each well was determined using the BCA protein quantification assay. 15 μL of the cell lysate was added to 200 μL of BCA reagent in a 96-well plate, and incubated at 37 °C for 30 min. The absorbance was measured at 562 nm with a microplate spectrophotometer and compared to a calibration curve prepared from known concentrations of bovine serum albumin.

For fluorescence imaging, cells were seeded onto 8-well chamber slides and treated with 200 μg mL^{-1} of FITC-labelled Arg/PAA-PSiNPs and NH_4OH/PAA-PSiNPs. After 4 h incubation, the cells were rinsed 5 times with PBS and transferred to heated stage at 37 °C for imaging using a confocal laser scanning microscope (Leica DMi8/SP8).

2.9 Statistical analysis

Results obtained from cell uptake experiments were analysed using the two-tailed Student's *t*-test to determine statistical significance. Differences between treatment groups were considered to be statistically significant when $P < 0.05$.

3. Results and discussion

3.1. Effect of isopropanol/water volume ratio on the formation and size of Arg/PAA polyelectrolyte droplets

In this study, oppositely charged PAA and Arg were first mixed in water at a molar ratio of 1:230 before the addition of IPA to induce formation of aqueous PEC droplets, which act as templates for the subsequent hydrolysis and condensation of silanes (Scheme 1). The influence of increasing the IPA volume on the formation and stability of the PECs was first investigated using dynamic light scattering (DLS) [30]. The correlation function curve, which is a plot of the intensity signal autocorrelation over a very short time scale, provides important information on the size and polydispersity of a particle suspension undergoing Brownian motion. To monitor colloid formation, the correlation function curves of Arg/PAA, NH_4OH/PAA, and PAA formed under different IPA volume fractions were collected. Figure S1 shows that for each PEC or PAA, a critical IPA volume is required for the formation of a stable particle suspension, which is characterised by a smooth, single exponential decay of the correlation function curve. For ease of interpreting the relationship and to explain the mechanisms involved in the IPA-induced colloid formation and stabilisation, a plot of the correlation function y-intercept against the IPA to water volume fraction is presented (Fig. 1A). The correlation function y-intercept gives an indication of the signal-to-noise ratio of the sample. A value closer to 1 indicates that the signal from a measured sample is high and taken together with the smooth exponential decays seen in correlation function curves shown in Figure S1, signifies that stable particles were formed. As seen from Fig. 1A, the correlation function y-intercepts of the Arg/PAA PECs remained approximately constant between 0.62 and 0.72 when the IPA volume fraction was increased from 0 to 50%. From 60 to 80% v/v IPA, a marked increase of the correlation function y-intercept to ~ 0.97 was observed, indicating that PECs with much greater stability were formed. A further increase in IPA to > 80% v/v resulted in the precipitation of the PECs. The complexation of the basic amino acid, Arg, with a polyanion such as polyoxometalates has been reported to occur *via* electrostatic interactions with the guanidinium group of Arg and salt-bridged hydrogen bonds between the α-NH_3^+ and α-COO^- of adjacent Arg molecules [31,32]. Due to the presence of excess Arg (acrylic acid monomer to Arg stoichiometric ratio = 1 : 9), the charged stabilised PECs are expected to be highly water soluble, with low solubility in IPA. As the dielectric constant of the binary mixture decreases with increasing IPA volume fractions [33], the electrostatic interaction parameter, which contributes to the solution free energy for the oppositely charged Arg and PAA, is enhanced as it is inversely proportional to $\varepsilon^{-3/2}$ [34,35]. This effectively promotes liquid–liquid phase separation of aqueous Arg/PAA PEC droplets which are stable and exist in equilibrium with the supernatant phase at a critical IPA volume of 60%.

A similar trend was observed with NH_4OH and PAA in which stable NH_4OH/PAA PECs were formed only between 80 and 99% v/v IPA (Fig. 1A and S1B). The lower IPA volume required to induce Arg/PAA PEC formation could be attributed to the higher cationic charge density of Arg and its ability to act as a crosslinker between anionic PAA chains, thus giving rise to stronger electrostatic interactions within the PEC. It is also worth noting that Arg/PAA PECs had higher correlation function y-intercept values than the 0.23–0.56 seen for NH_4OH/PAA at all concentrations below the critical IPA volumes, hence demonstrating that the Arg/PAA PECs formed were more stable. The behaviour of PAA alone with varying IPA/water volume fractions was also evaluated for comparison. Unlike the Arg/PAA and NH_4OH/PAA PEC systems, PAA undergoes liquid–liquid phase separation to form single component particles at much lower IPA volumes of 30–50% v/v (Fig. 1A and S1C). This phenomenon is due to a different mechanism in which the solubility

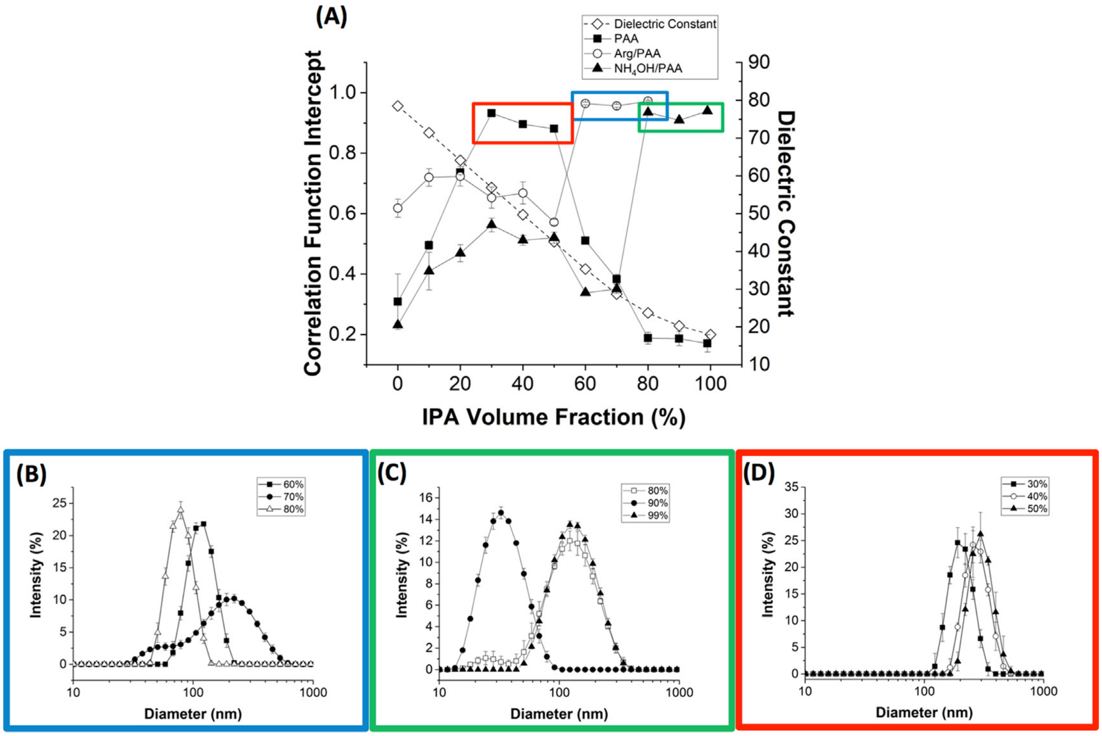

Fig. 1. Isopropanol (IPA)-induced formation and stabilisation of soluble polyelectrolyte complexes and PAA droplets. (A) Changes in the dynamic light scattering measured correlation function y-intercepts of Arg/PAA, NH_4OH/PAA, and PAA as a function of IPA volume and dielectric constant[37]. Intensity weighted size distributions of stable (B) Arg/PAA, (C) NH_4OH/PAA, and (D) PAA droplets formed at the critical range of IPA/water volume fractions corresponding to the coloured boxes shown in (A).

and conformation of PAA were affected by changes in solvent quality due to the complexation of the added IPA with water molecules [36]. Whilst PAA is separately soluble in water and IPA, its solubility is affected in the mixture. Initially, the PAA chains were ionised in water and were fully solvated due to hydrogen bonding with water. However, as more water/IPA complexes formed with the addition of increasing IPA volumes (0–30% v/v), PAA gradually becomes desolvated due to the reduced availability of free water molecules. This resulted in the stepwise increase in the signal-to-noise ratio or correlation function y-intercept observed (Fig. 1A). Despite the formation of water/IPA complexes, the water molecules remained in excess to solubilise the PAA chains. At a critical IPA range (30–50% v/v), the mixture is composed almost entirely of water/IPA complexes which are a poor solvent for PAA. The PAA droplets were thus the most stable with correlation function y-intercepts of > 0.8 and smooth correlation function curves obtained. Above this concentration, all the water molecules were sequestered within the water/IPA complexes and any additional IPA exists simply in bulk and is thus able to re-solubilise the PAA chains through enhanced hydrogen bonding. This results in the dissolution of PAA droplets and a decrease in the correlation function y-intercepts to baseline levels (~0.3) above 80% v/v IPA.

The size distributions of stable droplets obtained at the critical IPA volumes were further evaluated. As seen from Fig. 1B, monodisperse Arg/PAA PECs with hydrodynamic diameters of 113.7 ± 2.5 nm (polydispersity index, PDI = 0.03) and 76.6 ± 1.4 nm (PDI = 0.01) were obtained at 60 and 80% v/v IPA, respectively. This result contrasts favourably with the NH_4OH/PAA PECs, which had considerably broader size distributions with hydrodynamic diameters of 103.2 ± 0.83 nm (PDI = 0.23) and 121.9 ± 2.5 nm (PDI = 0.13) at 80 and 99% v/v IPA, respectively (Fig. 1C). As 80% v/v IPA yields stable PECs with comparable sizes in both Arg/PAA and NH_4OH/PAA, this solvent condition was selected for subsequent experiments investigating PEC size control and their use as templates for PSiNP synthesis. Although stable, narrowly dispersed colloids with hydrodynamic diameters ranging from 194 to 273 nm (PDIs of 0.04–0.11) were observed with PAA (Fig. 1D), the low pH of the reaction mixture renders the colloidal system unsuitable for use as templates for PSiNP synthesis (to be discussed in Section 2.3).

3.2. Effect of varying Arg, NH_4OH, and PAA on the size and dispersity of Arg/PAA and NH_4OH/PAA templates

As will be seen later, the size of the polyelectrolyte templates greatly affects the physicochemical and cancer cell targeting properties of the resultant PSiNPs. As such, we next investigated the influence of varying Arg, NH_4OH, and PAA on the size of the PEC colloidal templates. By keeping the PAA concentration constant, an increase in Arg from 2.0 to 30.8 mM led to an increment of Arg/PAA PEC sizes from 38.5 ± 0.1 to 72.0 ± 1.6 nm; with PDI remaining below 0.05 (Fig. 2A). As a corresponding pH rise from 6.5 to 9.5 with Arg addition was observed (Table 1), the greater deprotonation of carboxyl groups in PAA (pKa 4.5) [38] could have led to increased electrostatic interactions and sequestration of Arg as it is being added. The ability of Arg to crosslink adjacent PAA chains *via* electrostatic interactions and salt-bridged hydrogen bonding also further acts to enhance packing of more PAA and Arg, thereby resulting in the greater PEC diameters observed.

Similarly, increasing NH_4OH from 2.0 to 15.5 mM gave an increase in NH_4OH/PAA complex size from 70.3 ± 1.8 to 89.5 ± 0.3 nm but then followed by a decrease to 56.6 ± 1.0 nm for 30.8 mM NH_4OH (Figure S2A). The size distributions of the NH_4OH/PAA complexes were also significantly broader compared to the Arg/PAA complexes, with PDI values in excess of 0.24 over the range of NH_4OH tested (Figure S2B). The larger NH_4OH/PAA PEC sizes and PDIs observed could be attributed to the lower charge density of NH_4OH and absence of crosslinking ability compared to Arg. This effectively leads to diminished electrostatic interactions between NH_4OH and PAA, thus causing the PECs formed to be less stable and loosely packed. The resultant PECs thus have larger diameters and polydispersities.

The effect of varying PAA on the Arg/PAA template size was next investigated. PAA was found to have a greater influence on the size of the PECs formed at a fixed Arg concentration of 25.4 mM. As seen from Fig. 2B, increasing PAA concentration from 25 to 400 μM led to a greater diameter increase from 50 to 130 nm for the Arg/PAA PECs. The bigger size increase seen with varying PAA content could be due to the enhanced packing of PAA chains, which have much larger molecular weights than Arg, within the PECs. This finding is in agreement with the work by Nakashima *et al.* in which increased PAA/NH_4^+ aggregate sizes with increasing PAA con-

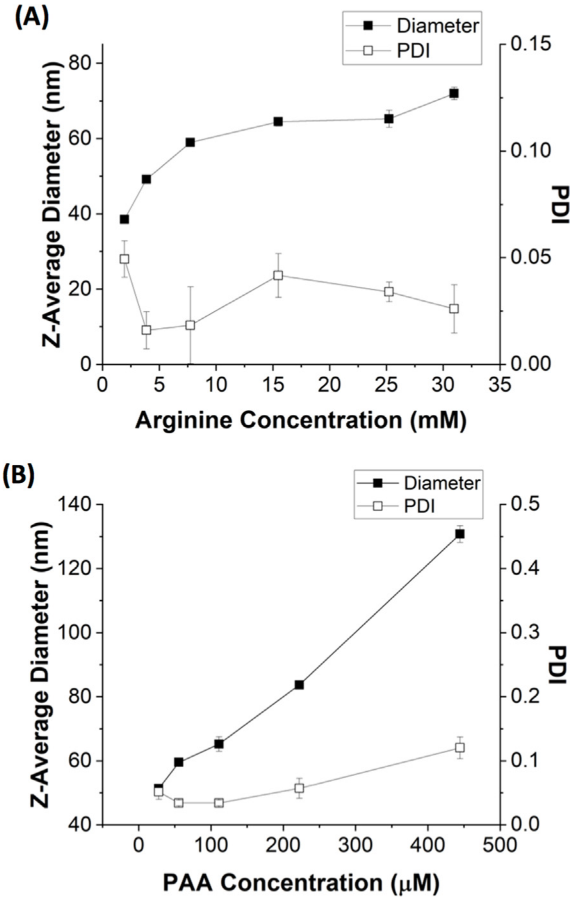

Fig. 2. Changes in the dynamic light scattering measured hydrodynamic diameters and polydispersity index of PECs formed by varying (A) Arg with PAA fixed at 111 μM, and (B) varying PAA with Arg fixed at 25.4 mM in 80% v/v IPA.

Table 1
pH values of PEC mixtures prepared with 2.0–30.8 mM of Arg or NH_4OH with a fixed 111 μM of PAA in 80% v/v solution of IPA in water.

Arg or NH_4OH concentration (mM)	pH of Arg/PAA PEC mixtures	pH of NH_4OH/PAA PEC mixtures
2.0	6.5	6.0
3.9	6.75	6.25
7.7	7.25	7.0
15.5	8.0	7.5
25.4	9.0	9.0
30.8	9.5	9.25

centrations in ethanol/water mixtures were observed [18]. Importantly, the low PDI values ranging from 0.02 to 0.05 were maintained through the significant size increase, hence presenting an efficient means to provide larger monodisperse colloidal templates for accessing larger functionalised PSiNPs.

3.3. Template directed porous silica nanoparticle synthesis

Upon identification of the optimal condition that leads to the formation of monodisperse PEC droplets, the Arg/PAA PECs were next investigated as colloidal templates for the hydrolysis and condensation of silanes to yield multifunctional PSiNPs. It was found previously that increasing Arg from 7.7 to 30.8 mM led to a pH increase in the reaction mixture from 7.25 to 9.5 (Table 1). As silane hydrolysis, condensation, and depolymerisation rates are higher at alkaline pH [39], we first evaluated the influence of Arg content, and hence the pH of the reaction mixture on PSiNP formation. TEM images of Arg/PAA-PSiNPs formed at a near neutral pH of 7.25 revealed that small, poorly defined clusters in addition to a dominant population of PSiNPs with an average diameter of 26 ± 3 nm were formed (Figure S3), suggesting the incomplete reaction of silica precursors within the 24 h reaction period. In contrast, single PSiNP populations ranging from 36 ± 3 to 50 ± 5 nm in diameter were obtained at a more alkaline pH of 8.0–9.5. To ensure complete reaction of the silanes and thus greater reproducibility, all further syntheses were performed at pH 9.0 with 25.4 mM of Arg.

The effect of varying the volume of the silica precursor triethoxysilane (TEOS) added to ~ 73 nm (by DLS) Arg/PAA PEC templates on the final PSiNP size and zeta-potential was subsequently studied. In general, an increase in TEOS volume from 20 to 500 μL led to a progressive increase in the size of the Arg/PAA-PSiNPs obtained (Fig. 3A). When 20 μL TEOS was added, Arg/PAA-PSiNPs with Z-average diameter of 61.3 ± 0.2 nm were obtained. This corresponded to approximately 85% of the original template diameter. The further addition of TEOS resulted in an overgrowth effect in which the size of the Arg/PAA-PSiNPs obtained exceeded the template size. For instance, at the highest TEOS volume of 500 μL, the PSiNPs obtained had a diameter of 255.6 ± 3.5 nm, which was 350% larger than the original PEC template diameter. The overgrowth of the PSiNPs beyond the PEC template diameter elicited a significant stepwise increase in PDIs from 0.05 to 0.17 (Fig. 3B). Consistent with the DLS results, TEM images confirmed that highly uniform and spherical Arg/PAA-PSiNPs with average diameters between 42 and 100 nm and with standard deviations of < 10% were obtained when 20–200 μL TEOS were added (Fig. 3C-E). The addition of 500 μL TEOS resulted in the largest PSiNPs with a size of 178 nm and with a standard deviation increase to 15%. These results clearly demonstrate the relationship between the colloidal template size and the amount of silane added on the size and uniformity of the Arg/PAA PEC templated PSiNPs obtained. A similar observation has also been made by Hu *et al.* where silica overgrowth brought about by an increase in silane mineralisation time with PAA/poly(L-lysine) PECs led to the formation of more dispersed silica nanoparticles with a loss of spherical morphology [11].

The zeta-potential of the Arg/PAA-PSiNPs in PBS (pH 7.4) was −27.9 ± 1.9 mV at 85% diameter of the colloidal template (Fig. 3B). This is likely due to the decoration of the PSiNP surface with Arg whose guanidinium and α-amino groups (pKa 12.1 and 9.0 respectively) [40] have positive charges, and PAA whose deprotonated carboxyl groups (pKa 4.5) impart a strongly negative surface charge [40,41]. PAA, however, extends from the surface like a brush partially covering the surface bound Arg and thus contributes more strongly to the zeta-potential under this growth regime (Scheme 2). The zeta potential increased to −7.0 ± 0.3 mV at 200% overgrowth. This result suggests a reduced surface presentation of the negatively charged PAA as the silica network filled the colloidal templates, although the Arg surface capping of the PSiNPs was retained due to the large excess of Arg present in the amino acid catalysed silica synthesis [42]. However, at the maximum TEOS volume of 500 μL which gave a PSiNP/template diameter ratio of 350%, a drastic drop in zeta-potential to −42.4 ± 2.0 mV was observed, suggesting that the particle surface was mainly comprised of deprotonated silanol groups without the presence of PAA or Arg. Beyond the addition of a critical amount of TEOS, the full occupation of the Arg/PAA PECs by the silica and complete consumption of the individual reagents in the drastically overgrowth regime plausibly led to the loss of surface functionalisation by these moieties. Taken together, these results demonstrate that to maintain the desired surface presentation of Arg and PAA on the PSiNPs, which have important consequences on cellular targeting effects, the amount of TEOS added needs to be optimised in order to obtain a PSiNP diameter that does not significantly exceed that of the template. Correspondingly, to access larger PSiNPs sizes that retain their monodispersity and surface functionality, the size of the Arg/PAA PEC template used could be increased according to the conditions discussed in section 2.2.

In contrast, the addition of 20–500 μL of TEOS to ~ 100 nm (by DLS) NH_4OH/PAA PECs templates did not give the same effect on the size and zeta-potential of the resultant PSiNPs obtained (Figure S4). The smallest TEOS volumes of 20 and 40 μL respectively gave the largest particles with hydrodynamic diameters of 112 and 153 nm (PDI 0.11 and 0.13) compared to 62 and 97 nm (PDI 0.05 and 0.08) for the Arg/PAA-PSiNPs. This is likely caused by template instability and resultant particle coalescence during synthesis due the inability of NH_4^+ to efficiently crosslink with PAA during PEC formation. Contrary also to Arg/PAA-PSiNPs, the TEOS volume added to the NH_4OH/PAA PECs showed no correlation with the zeta-potentials of the PSiNPs obtained, which were found to be between −30 to −40 mV independent of the particle growth regime (Figure S4). As will be seen later, the absence of PAA functionality within the NH_4OH/PAA-PSiNPs was confirmed with ATR-FTIR and TGA, hence the surface charge could be predominantly attributed to the surface silanol groups. Notably, the zeta-potential value of the significantly overgrown Arg/PAA-PSiNPs (PSiNP/template diameter ratio of 350%) is close to the values obtained for the NH_4OH/PAA-PSiNPs, suggesting the lack of surface PAA or Arg functionality discussed above.

For the successful clinical translation of the Arg/PAA-PSiNPs as drug carriers, the scalability and reproducibility of the synthesis are imperative. The simple one-pot synthesis method can be reproducibly scaled-up 25-fold to a 250 mL volume (mass yield ~ 100 mg) with no detrimental effects to the particle size, morphology, or monodispersity (Figure S5). The Z-average diameters of the Arg/PAA-PSiNPs obtained from 3 different scaled up batches were found to have a very small variation of < 5 nm (Figure S5C). In contrast, PSiNPs synthesised with NH_4OH/PAA colloidal PEC templates were found to have much poorer size uniformity and reproducibility with Z-average diameters ranging from 73 to 151 nm across 3 batches (Figure S6). This could be explained by the broader size distribution of the NH_4OH/PAA PECs (Fig. 1C), which results in the non-uniform deposition and growth of porous silica to cause significant size variations between batches. These results underscore the benefits of using Arg/PAA PECs as templates for producing highly uniform PSiNPs for biomedical applications.

3.4. Characterisation of Arg/PAA-PSiNPs and NH_4OH/PAA-PSiNPs

The chemical functional groups of the Arg/PAA-PSiNPs and NH_4OH/PAA-PSiNPs were characterised by ATR-FTIR and TGA. For both

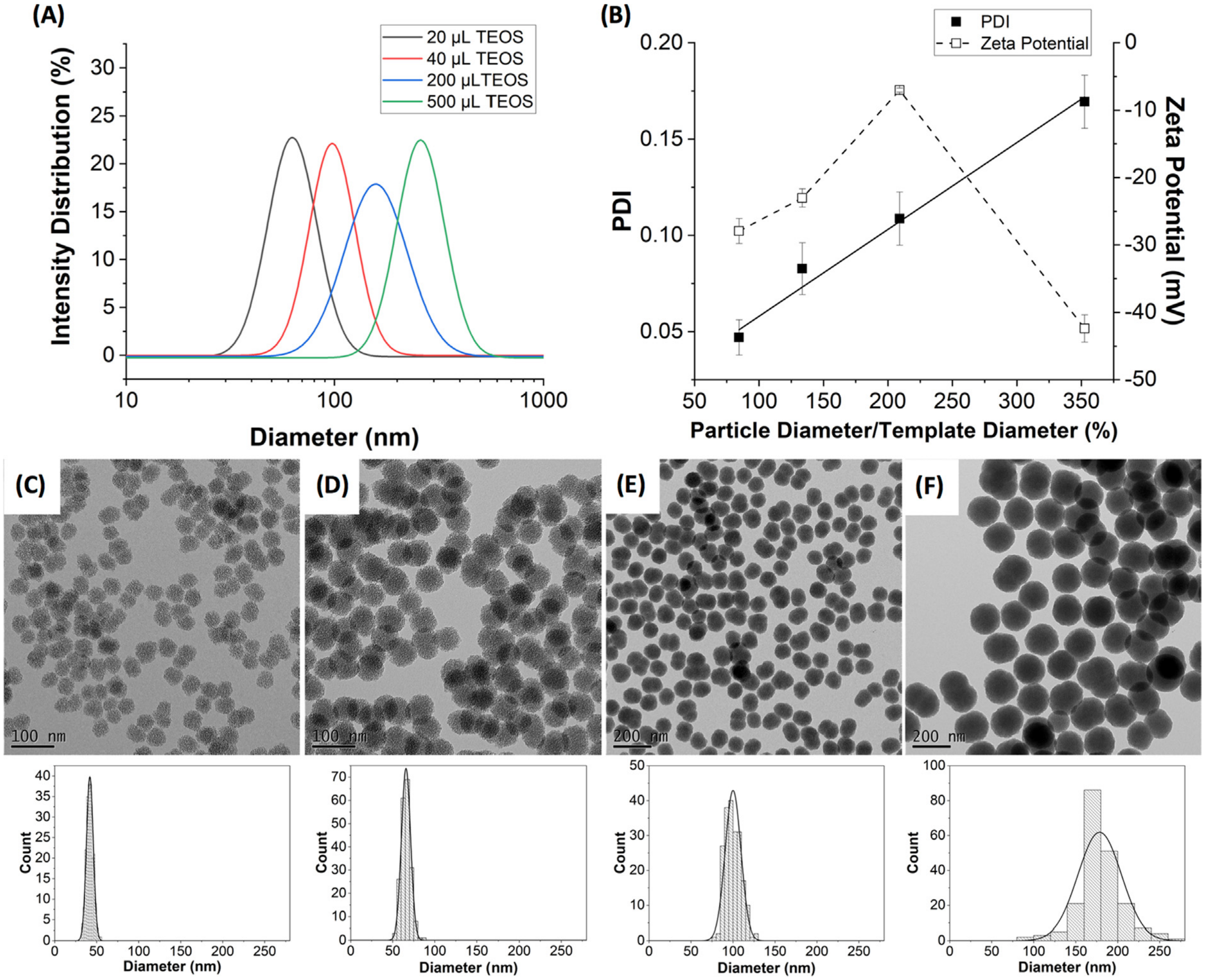

Fig. 3. (A) Intensity weighted DLS size distributions of the Arg/PAA-PSiNPs displayed in (C-F) with Z-average diameters of 61.3 ± 0.2 nm, 96.9 ± 2.6 nm, 151.6 ± 1.6 nm, and 255.6 ± 3.5 nm synthesised with 20, 40, 200, and 500 µL TEOS respectively. (B) The polydispersity index and zeta-potentials of the Arg/PAA-PSiNPs expressed shown in (A) as a function of the ratio of the particle and the polyelectrolyte template diameter showing the effect of the under- and over-growth regimes. TEM images and diameter histograms for Arg/PAA-PSiNPs synthesised by adding (C) 20, (D) 40, (E) 200, and (F) 500 µL of TEOS to 70 nm (by DLS) polyelectrolyte colloidal templates. The average diameters determined from the TEM images are (C) 42 ± 4 nm, (D) 66 ± 5 nm, (E) 100 ± 9 nm, and (F) 178 ± 28 nm, respectively (n = 200).

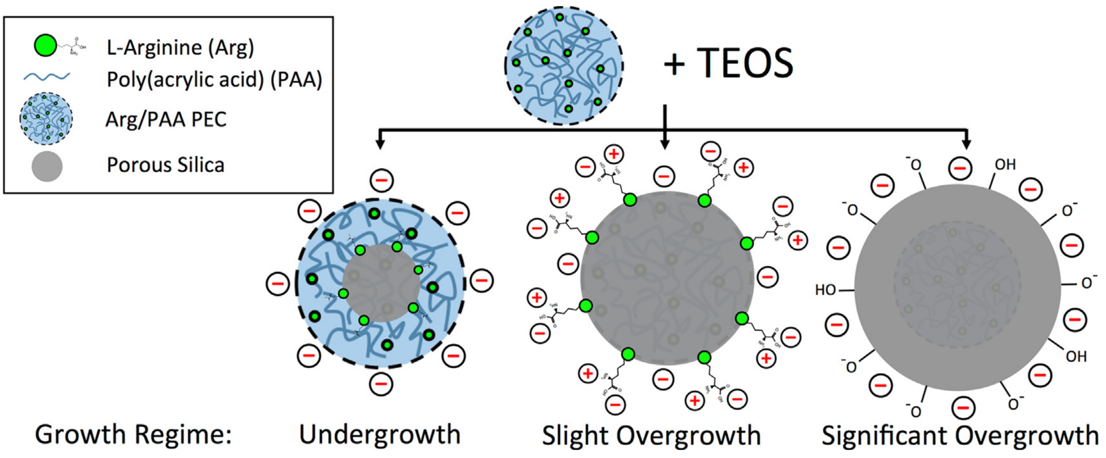

Scheme 2. A schematic depiction of the three possible undergrowth and overgrowth regimes and their impact on surface functionality.

particle types, typical silica vibration modes corresponding to Si–O–Si asymmetric stretching as well as Si–O and Si–OH stretching were observed at 1000–1250, 794, and 935 cm^{-1}, respectively (Fig. 4A) [43]. The presence of Arg on the Arg/PAA-PSiNP was confirmed from the presence of common vibrational modes in the Arg and Arg/PAA-PSiNP spectra. The absorption bands which correspond to asymmetric –NH– bending, asymmetric –C—O– stretching, and symmetric –C—O– stretching were observed at

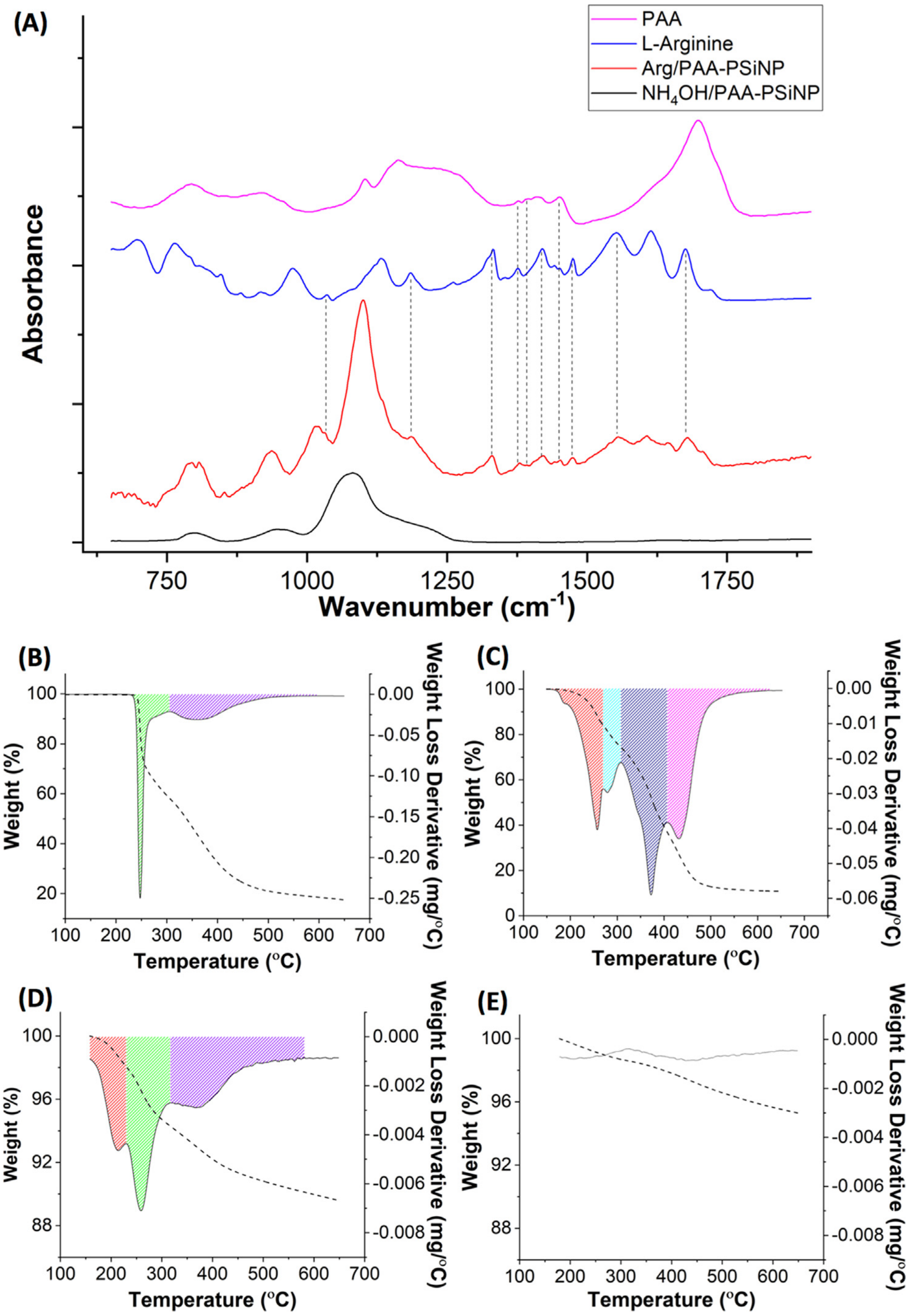

Fig. 4. Chemical characterisation of Arg/PAA-PSiNPs and NH_4OH/PAA-PSiNPs. (A) Stacked ATR-FTIR spectra showing the fingerprint regions for PAA, Arg, Arg/PAA-PSiNP, and NH_4OH/PAA-PSiNP. TGA curves and the 1st derivatives of the weight loss curves for (B) Arg, (C) PAA, (D) Arg/PAA-PSiNPs and (E) NH_4OH/PAA-PSiNPs, where coloured peaks indicate the presence of a common organic compound between samples.

1675, 1558, and 1475 cm^{-1}, respectively for Arg [25,44], and at 1679, 1555, and 1474 cm^{-1} for Arg/PAA-PSiNPs. Although the in-plane –C—O—H bending, asymmetric CH_2 stretching, and C=O stretching modes typical of PAA appeared at 1413, 1450, and 1698 cm^{-1} in the Arg/PAA spectra, they also coincide with peaks assigned to Arg [45]. Furthermore, broad peaks for the CH_2 rocking and C—O symmetric stretching occurring at 792 and 918 cm^{-1} for PAA also coincide with the sharper peaks for Si–O and Si–OH stretching, thus preventing conclusive confirmation of PAA functionalisation in the PSiNPs using ATR-FTIR. As such, TGA was further employed as a complementary technique to confirm the presence of PAA. The absorption spectrum for NH_4OH/PAA-PSiNPs showed comparatively fewer spectral features. As expected, none of the peaks attributed to Arg were present and the above discussed in-plane –C—O—H bending, asymmetric CH_2 stretching, and C=O stretching for PAA peaks were also not observed, hence indicating the absence of both Arg and PAA functionality on the NH_4OH/PAA-PSiNPs. TGA analyses further confirmed the retention of PAA and Arg functionality within Arg/PAA-PSiNPs whereas no detectable organic functionality was observed for NH_4OH/PAA-PSiNPs. The thermal degradation profile of Arg/PAA-PSiNPs revealed distinct weight loss peaks beginning at 229 and 316 °C which were close to the 220 and 305 °C observed for Arg (Fig. 4B), thus indicating the presence of Arg within the PSiNPs. The existence of PAA within the Arg/PAA-PSiNPs was confirmed through the appearance of a weight loss peak at around 157 °C which was close to that observed at 149 °C for PAA alone (Fig. 4C and D). Consistent with the ATR-FTIR data, no discernible weight loss ascribed to the presence of PAA was found with the NH_4OH/PAA-PSiNPs (Fig. 4E). It is thus evident that electrostatic interactions between NH_4^+ and PAA were not sufficient to retain the polymer during the repeated washing steps used to remove excess reagents. Wan and Yu. have also previously reported a similar result in which PAA was found to be completely removed from hollow silica nanoparticles templated from PAA/NH_4^+ in ethanol solutions by washing [16]. Conversely, the increased charge density and efficient crosslinking ability of Arg enhances packing and retention of PAA in the PECs and the final PSiNP product, which will be seen later to contribute greatly to the increased porosity and pH responsive drug release capabilities of the Arg/PAA-PSiNPs.

To determine the surface area and porosity of the Arg/PAA-PSiNPs and NH_4OH/PAA-PSiNPs, N_2 adsorption–desorption measurements was performed. From Fig. 5A, the N_2 adsorption–desorption isotherms of both types of PSiNPs displayed a characteristic type IV behaviour, with the presence of type H3 hysteresis loops which indicates the presence of porous structures. The surface area of Arg/PAA-PSiNP determined using BET analysis was found to be 548.7 m^2/g. Pore size distributions of the Arg/PAA-PSiNPs determined using NLDFT analysis showed pore diameters ranging from 1.1 to 2.7 nm, with a dominant peak at 1.8 nm, clearly demonstrating the presence of disordered pore structures (Fig. 5B). The corresponding data for NH_4OH/PAA-PSiNP displayed pore distributions over a comparable diameter size range, but with significantly reduced pore volumes, and a lower BET surface area of 117.5 m^2/g. As previously discussed, the increased charge density and crosslinking ability of Arg leads to greater retention of PAA chains during the hydrolysis and condensation of silane species and the presence of this polyelectrolyte network gives rise to the particle porosity. This is consistent with the reduced electrostatic interaction between NH_4OH and PAA and the resulting poor polymer retention within the PECs which ultimately leads to reduced surface area and porosity for NH_4OH/PAA-PSiNPs.

The colloidal stability of the Arg/PAA-PSiNPs were evaluated in water, PBS (pH 7.4), and cell culture media by DLS. As seen in Figure S7, no significant changes in the Z-average diameters and size distributions were observed in different physiologically relevant conditions, thus demonstrating their excellent colloidal stability.

3.5. Drug loading and release of doxorubicin hydrochloride

The drug loading and pH responsive drug release capabilities of the polyelectrolyte templated PSiNPs were investigated using Dox. The Arg/PAA-PSiNPs were found to have significantly higher drug loading capacity compared to the NH_4OH/PAA-PSiNPs at 1 and 2 mg/mL initial Dox loading concentrations (Fig. 6A; $P < 0.05$). With the Arg/PAA-PSiNPs, the highest drug loading capacity of 22% w/w was achieved at 1 mg/mL of initial Dox, which is comparable to that achieved with other porous silica nanoparticles [46–50]. Although several examples of polymer grafted porous silica particles have exhibited higher loading capacities sometimes in excess of 50%, this is likely due to interaction of Dox and with exterior polymer chains which reduces the possibility for adding targeting or secondary surface functionality [51–53]. A stepwise reduction in drug loading capacity to 16 and 8% w/w at higher Dox concentrations of 2 and 4 mg/mL, respectively was also observed. In contrast, the NH_4OH/PAA-PSiNPs showed a maximum drug loading capacity of only 8% w/w at 1 mg/mL Dox. The higher drug loading capacity of the Arg/PAA-PSiNPs could be attributed to the higher anionic PAA retention afforded by the presence of Arg within the PECs as confirmed earlier by TGA (Fig. 4D). This permits enhanced electrostatic interaction with the cationic Dox to give higher drug encapsulation capacity within the pores of the Arg/PAA-PSiNPs. The hydrodynamic diameters of the Dox-loaded Arg/PAA-PSiNPs and NH_4OH-PSiNPs were found to be 162.4 ± 3.4 and 152.2 ± 0.2 nm, respectively, which were higher than the initial 128.4 ± 2.4 and 132.1 ± 0.1 nm of the respective empty PSiNPs (Figure S8A). This result suggests that some amount of cationic Dox was also adsorbed on the surface of the anionic PSiNPs *via* electrostatic interactions with surface silanol groups and PAA. Indeed, the Dox-loaded Arg/PAA-PSiNPs and NH_4OH/PAA-PSiNPs were found to have zeta-potentials of −16.0 ± 0.7 and −19.0 ± 0.9 mV, respectively, which were higher than the −24.6 ± 1.1 and −36.9 ± 4.8 mV observed for empty PSiNPs (Figure S8B), hence indicating the presence of positively charged Dox on the surface. A significantly higher drug loading was observed with the Arg/PAA-PSiNPs compared to the NH_4OH/PAA-PSiNPs. In the case of the latter, a significant proportion of the loaded Dox was likely to have been adsorbed on the exterior surface, whilst the majority of Dox retained by Arg/PAA-PSiNPs was contained within the pores with a smaller amount adsorbed on the surface. This conjecture is supported by the BET and NLDFT data described earlier in which the dominant pore size for Arg/PAA-PSiNPs was 1.8 nm. This was sufficiently large for the loading of Dox, which has a maximum diameter of 1.5 nm [53]. The smaller pore volumes and peak pore

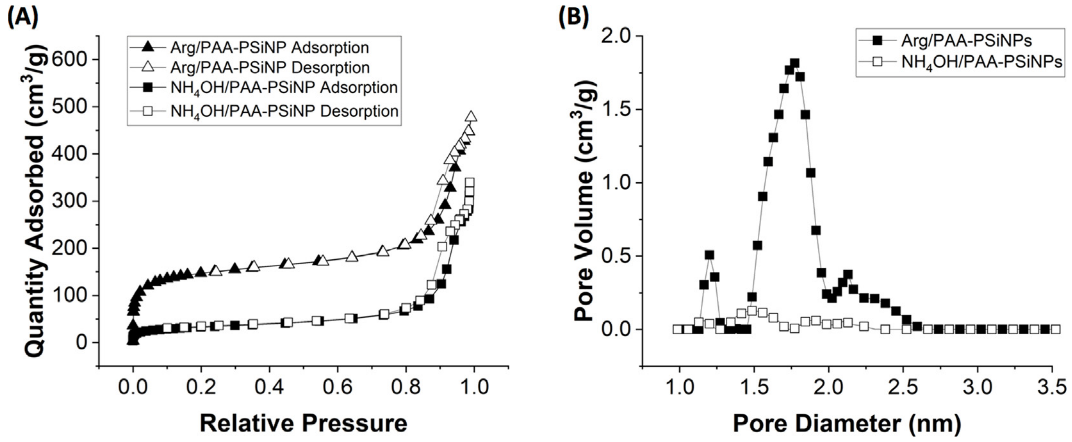

Fig. 5. (A) N_2 gas adsorption/desorption isotherms collected at 77 K for Arg/PAA-PSiNPs and NH_4OH/PAA-PSiNPs and (B) the corresponding pore size distributions determined using non-local density function theory analysis.

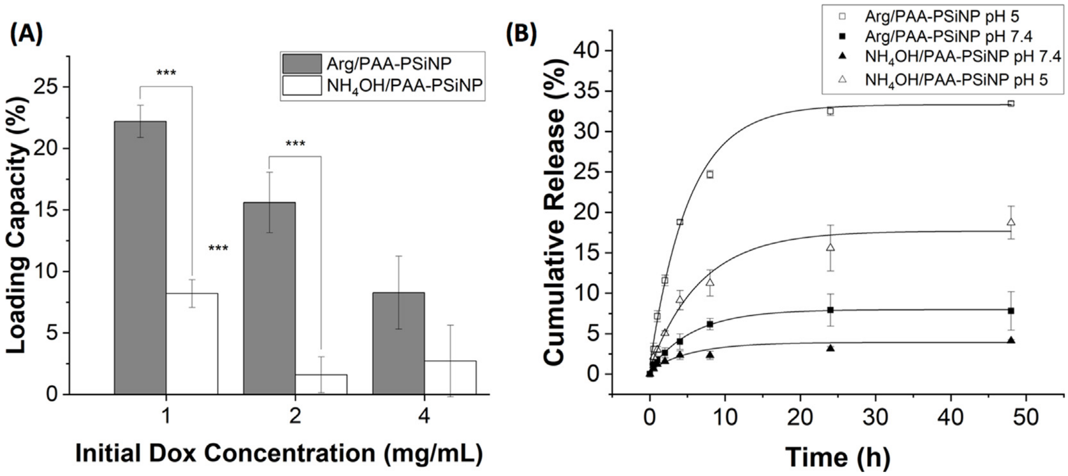

Fig. 6. (A) Drug loading capacity of Arg/PAA-PSiNPs and NH_4OH/PAA-PSiNPs (1 mg/mL) incubated with 1, 2, and 4 mg/mL Dox for 48 h. (B) Cumulative Dox release from the Arg/PAA-PSiNPs and NH_4OH/PAA-PSiNPs over 48 h in PBS (pH 7.4) and sodium acetate buffer (pH 5.0). The results represent mean ± standard deviation from 3 independent experiments.

diameter of 1.5 nm for the NH_4OH/PAA-PSiNPs led to reduced loading and retention of drug within the pore network compared to the Arg/PAA-PSiNPs.

An added benefit of incorporating PAA within the colloidal templates used for the synthesis of PSiNPs is the ability to provide stimuli-responsive drug release in response to an acidic tumour microenvironment and/or endosomal environment following cellular uptake. As the carboxylic acid groups in PAA have a pKa of 4.5, they are predominantly deprotonated at the physiological pH of 7.4, leading to the extension of the polymer chains into the pores due to electrostatic repulsion. This effectively enhances the interaction and retention of the Dox by the extended PAA chains within the pores of the Arg/PAA-PSiNPs. Under acidic pH, however, the protonation of PAA's carboxylic acid groups leads to reduced interaction between PAA chains and the Dox, thus facilitating drug release from the PSiNPs. As depicted in Fig. 6B, the Arg/PAA-PSiNPs were found to have a significantly higher drug release of 33.3% in sodium acetate buffer (pH 5.0) compared to only 8% in PBS (pH 7.4) over 48 h. The low levels of Dox released at physiological pH could be attributed to charge screening effects by ions in the PBS to reduce electrostatic interactions between the adsorbed drug with deprotonated PAA and/or surface silanol groups. Although a similar pH-responsive Dox release profile was also observed with the NH_4OH/PAA-PSiNPs, it is important to note that the maximum drug release attained at pH 5.0 was much lower at 17.4%. The enhanced Dox release from the NH_4OH/PAA-PSiNPs under acidic pH is likely to be due to the fact that most of the Dox molecules were adsorbed on the surface through electrostatic interaction with surface silanol groups (pKa 4.5) [54], and thus a decrease in pH to 5.0 leads to the partial protonation of the silanol groups and Dox displacement from the surface of the PSiNPs. The absence of PAA in the NH_4OH/PAA-PSiNPs was confirmed earlier by TGA, thus the mechanism of drug loading and release is ascribed to electrostatic interactions between the surface silanol groups and cationic Dox.

The *in vitro* drug release kinetics and mechanisms at different pH were further evaluated using the Korsmeyer-Peppas model [27]. Good linearity with high correlation coefficients (R^2) of > 0.98 were found for all the samples thus indicating the appropriateness of this model for evaluating the drug release kinetics (Figure S9 and Table 2). As discussed previously, the increased protonation of PAA chains within the Arg/PAA-PSiNPs with a decrease in pH from 7.4 to 5.0 leads to greater and faster drug release in acidic pH. Indeed, a rise in the kinetic constant, k_m from 1.78 to 6.84 was seen with the Arg/PAA-PSiNPs, hence indicating more rapid drug release in acidic pH (Table 2). In contrast, a smaller increase in the k_m from 1.05 to 3.11 was observed for the NH_4OH/PAA-PSiNPs with pH reduction (Table 2). This result indicates that a slower rate of drug release from the NH_4OH/PAA-PSiNPs is occurring in acidic pH possibly *via* the pH-dependent displacement of surface adsorbed Dox. The release exponent, n, was found to range from 0.58 to 0.73 for all samples, hence indicating that the drug release from the Arg/PAA-PSiNPs and NH_4OH/PAA-PSiNPs occurred by non-Fickian diffusion ($n > 0.43$) involving both diffusion and polymer swelling. Although PAA was only detected in the Arg/PAA-PSiNPs and not in the NH_4OH/PAA-PSiNPs (Fig. 4), the similar n values observed for both particle types at the same pH suggest a diffusion mechanism that is dependent on pH and electrostatic interactions (Table 2).

3.6. In vitro biosafety and selective uptake of Arg/PAA-PSiNPs by primary human glioblastoma cells

The biosafety and uptake of the Arg/PAA-PSiNPs and NH_4OH/PAA-PSiNPs were assessed using two different patient-derived GBM cell lines, GBM1 and GBM20. The GBM1 cell line was derived from a primary tumour with no prior treatment and the GBM20 cell line originated from recurrent GBM post radiotherapy, temozolomide, and IMA950 treatment [28,29]. Both cell models exhibit stem cell-like features as well as transcriptional heterogeneity at the single cell level representing classical, proneural, and mesenchymal GBM tumour cell subpopulations. In addition, the non-tumorigenic human adult neural progenitor cell line, NP1, derived from primary tissue obtained from a patient undergoing epileptic surgery, was included as a control [28,29]. The cytotoxicity of the Arg/PAA-PSiNPs and NH_4OH/PAA-PSiNPs towards the various cell lines was first evaluated using the WST-1 assay. No significant cytotoxicity was observed in GBM1 and NP1, with > 80% cell viability observed up to high concentrations of 750 μg/mL after 24 h treatment (Fig. 7A and C). Although a slight dose-dependent toxicity was observed in GBM20, the cell viability remained $\geq$ 77% up to a supraphysiological concentration of 250 μg/mL, which was much higher than the concentrations used in subsequent cellular uptake and drug delivery studies. As Arg/PAA-PSiNPs and NH_4OH/PAA-PSiNPs have similar cytotoxicity profiles in GBM20 at high concentrations, it is likely that the induced cyctotoxicity observed is intrinsic of silica nanoparticles and is not due to the added Arg or PAA surface functionality.

Table 2
The release exponent, *n*, and kinetic constant, k_m, describing the pH responsive release kinetics, and R^2 values for Arg/PAA-PSiNPs and NH_4OH/PAA-PSiNPs.

Particle type	pH of release medium	*n*	k_m	R^2
Arg/PAA-PSiNPs	5	0.73 ± 0.04	6.84 ± 0.08	0.996
	7.4	0.58 ± 0.01	1.78 ± 0.01	0.999
NH_4OH/PAA-PSiNPs	5	0.72 ± 0.06	3.11 ± 0.07	0.988
	7.4	0.61 ± 0.01	1.05 ± 0.03	0.981

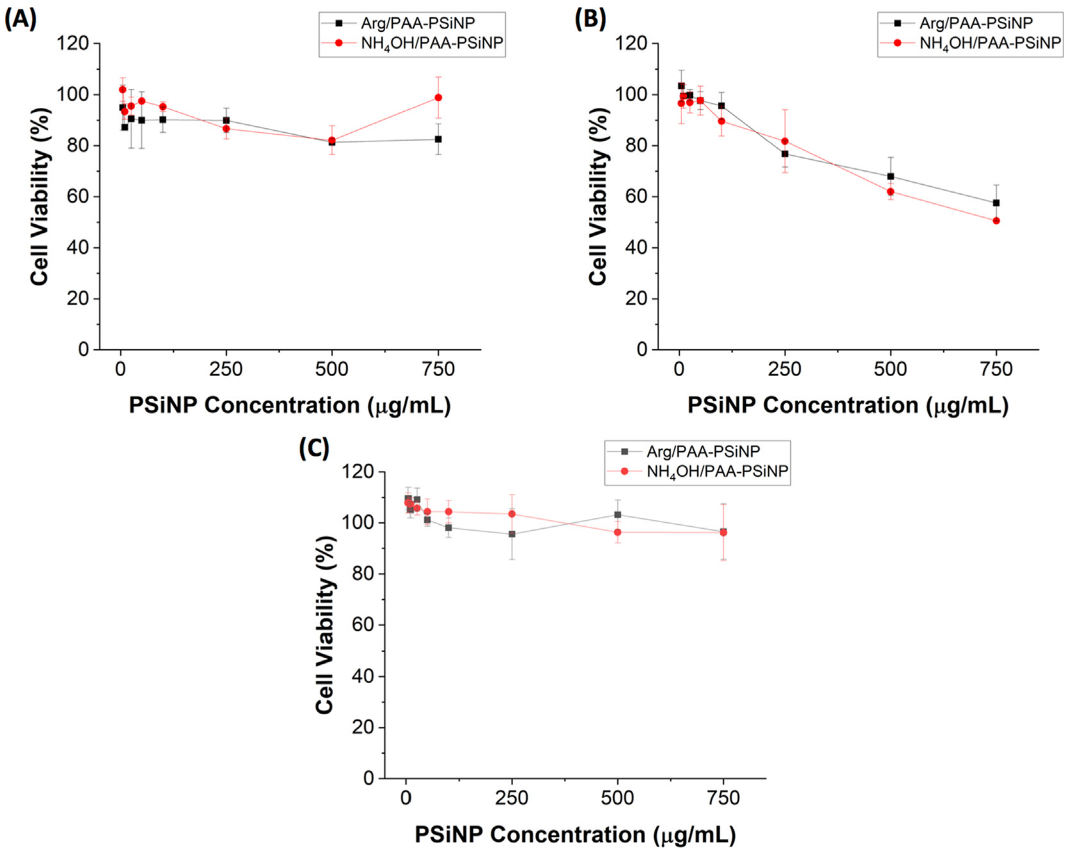

Fig. 7. Cytotoxicity of Arg/PAA-PSiNPs and NH_4OH/PAA-PSiNPs in patient-derived glioblastoma cell lines. Graphs show cellular viability of GBM1 (A), GBM20 (B), and the (C) non-tumourigenic human adult neural progenitor NP1 cells treated with 0–750 μg/mL of Arg/PAA-PSiNPs and NH_4OH/PAA-PSiNPs for 24 h. The results represent mean ± standard deviation from at least 2 independent experiments performed with six replicates.

To assess the tumour cell selectivity, fluorescent FITC-labelled Arg/PAA-PSiNPs and NH_4OH/PAA-PSiNPs were synthesised by the co-condensation of FITC-PEG-silane with TEOS. By varying the volume of silanes added, the diameters of the FITC-labelled Arg/PAA-PSiNPs were readily tuned between 22.8 ± 2.3 nm–83.9 ± 9.7 nm; with narrow size distributions obtained (Figure S10A-C). The FITC-labelled Arg/PAA-PSiNPs demonstrated strong absorbance at 490 nm, with a clear fluorescence emission peak at 518 nm with excitation at 490 nm (Figure S10D-E). GBM1, GBM20, and NP1 cells were incubated with FITC-labelled Arg/PAA-PSiNPs and NH_4OH/PAA-PSiNPs with comparable Z-average diameters of 112.9 ± 2.2 and 127.6 ± 2.6 nm, respectively for 24 h. After removal of non-internalised PSiNPs, the cells were lysed and quantified for cellular uptake using fluorescence spectrometry. To account for differences in cell number and size between cell lines, the fluorescence intensity values obtained were normalised for protein expression determined by BCA assay. A significantly higher uptake of Arg/PAA-PSiNPs compared to the non-targeting NH_4OH/PAA-PSiNPs was observed in both GBM cell models (Fig. 8A; $P < 0.001$); with a 2.9- and 3.7-fold higher uptake of Arg/PAA-PSiNPs in GBM1 and GBM20, respectively. Notably, there was no significant difference in uptake of Arg/PAA-PSiNPs and NH_4OH/PAA-PSiNPs in the non-tumourigenic NP1 cells ($P > 0.05$). To further confirm the cellular internalization of the Arg/PAA-PSiNPs and NH_4OH/PAA-PSiNPs, confocal imaging of the GBM20 and NP1 cells was performed. Consistent with the cellular uptake data, GBM20 cells treated with the cancer targeting Arg/PAA-PSiNPs exhibited stronger fluorescence intensities compared to the non-targeting NH_4OH/PAA-PSiNPs and Arg/PAA-PSiNP treated non-tumourigenic NP1 cells (Fig. 8). No apparent difference in fluorescence intensities between confocal images of NP1 cells treated with Arg/PAA-PSiNP and NH_4OH/PAA-PSiNPs was observed. Z-stack imaging of the Arg/PAA-PSiNP treated GBM20 cells confirmed that the nanoparticles were internalised by the cells and were not simply adhered to the surface of the cells (Movie S1). These results demonstrate a marked enhancement of cellular uptake capabilities of the Arg/PAA-PSiNPs towards the GBM cells over non-tumourigenic NP1 cells, thus demonstrating their potential for use as selective cancer targeted drug delivery vehicles.

3.7. Effect of Arg/PAA-PSiNP overgrowth on cellular uptake

As discussed earlier, the increased addition of TEOS to the initial PEC template to obtain significantly overgrown Arg/PAA-PSiNPs

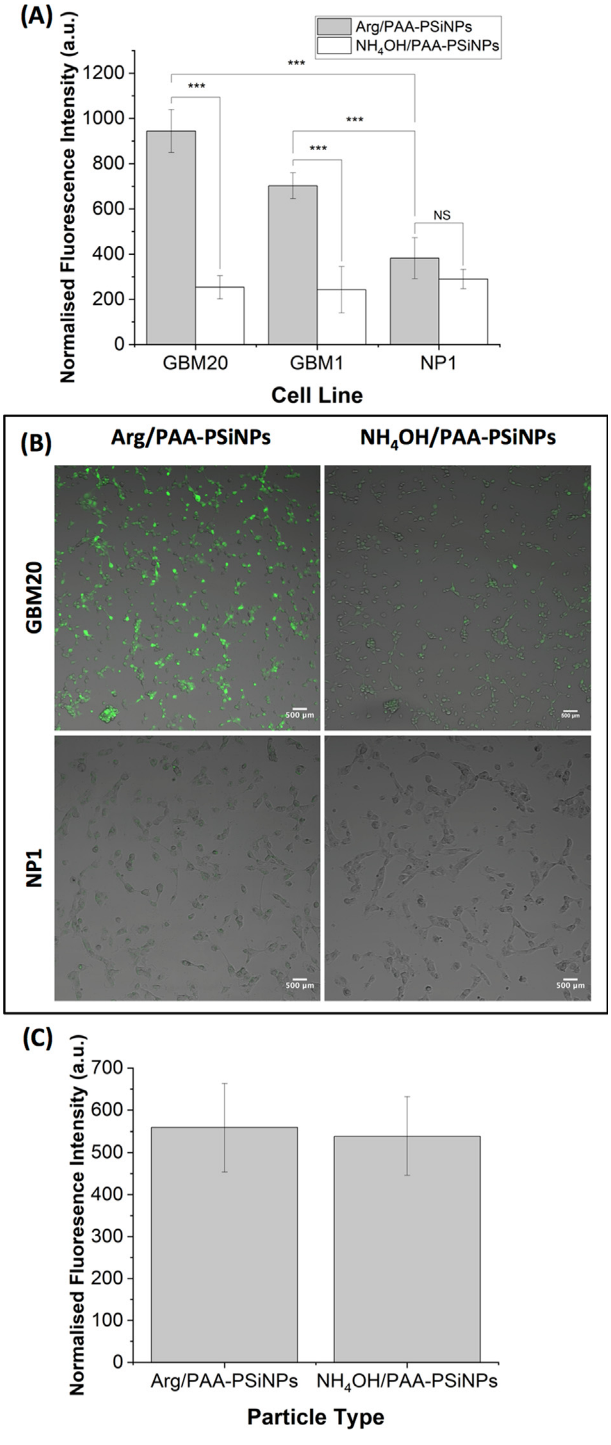

Fig. 8. Enhanced targeting and uptake of Arg/PAA-PSiNPs by patient-derived glioblastoma cells. (A) Cellular uptake of FITC-labelled Arg/PAA-PSiNPs and NH_4OH/PAA-PSiNPs after treating GBM1, GBM20, and non-tumourigenic neural progenitor NP1 cells with 200 μg/mL of PSiNPs for 4 h. The fluorescence intensities of the internalized particles were normalized for cellular protein content using the bicinchoninic acid assay. Each data point represent mean ± standard deviation from at least two independent experiments performed with six replicates. *** $P < 0.001$; NS indicates lack of statistical significance ($P > 0.05$). (B) Confocal images of GBM20 and NP1 cells following treatment with FITC-labelled Arg/PSiNPs and NH_4OH/PAA-PSiNPs. (C) Cellular uptake of overgrown FITC-labelled Arg/PAA-PSiNPs and NH_4OH/PAA-PSiNPs by GBM20 cells performed in triplicate.

(final PSiNP/template diameter ratio of 350%) led to a drastic drop in zeta-potential to −42.4 ± 2.0 mV (Fig. 3B), which was indicative of deprotonated silanol groups at a particle surface devoid of Arg functionalisation. The cellular uptake of the significantly overgrown Arg/PAA-PSiNPs was thus further investigated using GBM20 cells. Compared to the Arg/PAA-PSiNPs synthesised with 40 μL of TEOS (PSiNP/template diameter ratio of 157%) which have shown tumour specific targeting earlier (Fig. 8A), a significant decrease in the normalised fluorescent intensity from 933 a.u. to 558 a.u. was seen, thus demonstrating a reduced cellular uptake of the overgrown Arg/PAA-PSiNPs. Importantly, a direct comparison of the cellular uptake of overgrown Arg/PAA-PSiNPs and NH_4OH/PAA-PSiNPs with comparable hydrodynamic diameters of 226.3 ± 6.4 and 194.3 ± 2.9 nm, respectively (Figure S11), did not give a significant difference in cellular uptake ($P > 0.05$; Fig. 8C). This result clearly indicates a loss of cancer targeting abilities when Arg/PAA-PSiNPs were prepared in a drastically overgrown regime from the initial PEC colloid template. When small amounts of TEOS were added, sufficient Arg and PAA remained available within the colloidal system to present on the surfaces of the Arg/PAA-PSiNPs formed. Beyond the addition of a critical amount of TEOS, most of the Arg and PAA in the system were likely to have been used up as scaffolds for the hydrolysis and condensation of the silanes, hence resulting in the formation of PSiNPs with minimal or no Arg surface functionalisation for cancer targeting (Scheme 2). Taken together, these results strongly highlight the need to consider appropriate colloidal template sizes for the preparation of polyelectrolyte templated PSiNPs used in cancer targeting applications to ensure that the cell targeting moieties are retained on the surface of the final products. It is plausible that to obtain larger monodisperse PSiNPs that retain the surface presentation and hence functional properties of each polyelectrolyte used in the PECs, correspondingly larger colloidal templates would need to be used in the synthesis.

3.8. Enhanced anticancer efficacy in patient-derived glioblastoma cells

The anticancer drug delivery potential of the Arg/PAA-PSiNPs with combined tumour targeting and pH-responsiveness was demonstrated using patient derived GBM1 cells. The enhanced tumour cell uptake and increased Dox release in acidic pH environments such as the weakly acidic endosomes following cellular internalisation effectively led to a significantly reduced half maximal inhibitory concentration (IC_{50}) of 5.3 μM with Dox-loaded Arg/PAA-PSiNPs compared to 14.0 μM of NH_4OH/PAA-PSiNPs (Fig. 9) in cell viability assays. The observed IC_{50} value of Dox-loaded Arg/PAA-PSiNPs equates to 13.2 μg/mL of empty Arg/PAA-PSiNPs, which is a concentration previously shown to induce minimal or no toxicity in GBM1 cells (Fig. 7B). This result clearly demonstrates that the enhanced anticancer effect seen with Dox-loaded Arg/PAA-PSiNPs was due to the anticancer drug released and not a result of PSiNP induced toxicity. The higher IC_{50} value observed with Dox-loaded Arg/PAA-PSiNP compared to free Dox (1.8 μM) can be explained by the slower drug release, where only approximately 30% of the loaded Dox was released from the Arg/PAA-PSiNPs after 24 h (Fig. 6B). In spite of this result, the strong tumour cell selectivity and pH-responsiveness of the Arg/PAA-PSiNPs are expected to be more advantageous to promote *in vivo* tumour accumulation of the Dox-loaded Arg/PAA-PSiNPs, where enhanced Dox release can occur in response to the acidic tumour microenvironment and in the endosomes following uptake by tumour cells.

4. Conclusion

Advancing from previously reported protocols [11,20], we have introduced a versatile means to obtain highly uniform sub-100 nm PSiNPs with readily tunable sizes using colloidally stable Arg/PAA PECs as soft templates for silane mineralisation. We first

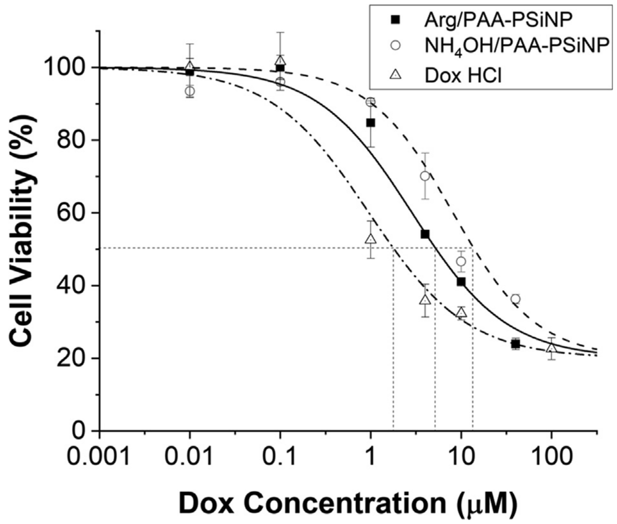

Fig. 9. Cell viability of GBM1 cells following 24 h treatment with Dox-loaded Arg/PAA-PSiNPs and NH_4OH-PSiNPs as determined using the WST-1 assay. The dotted lines indicate the IC_{50} values. The results represent mean ± standard deviation from two independent experiments performed with six replicates.

demonstrated that the strong electrostatic interactions between Arg with PAA not only improved PEC uniformity compared to NH_4OH/PAA PECs, and enabled fine control of the template diameter, but also led to greatly increased porosity in the PSiNPs without the need for template removal. The retention of PAA in the porous network considerably enhanced the loading and pH responsive release of anticancer therapeutic Dox. Additionally, Arg acted as a basic catalyst and capping agent in the hydrolysis and condensation of silane precursors leading to facile surface functionalisation of the PSiNPs during synthesis. We subsequently demonstrated that the relationship between the volume of added silane and the PEC template size could readily control the particle diameter and monodispersity, and was further used to vary the surface presentation of cancer-targeting molecule, Arg. The selective uptake and tumoricidal activity of Dox-loaded Arg/PAA-PSiNPs were successfully demonstrated using primary patient-derived GBM cells in comparison with non-tumorigenic neural progenitor cells. Taken together, this readily scalable one-pot synthesis method of obtaining highly uniform sub-100 nm PSiNPs with desirable properties such as pH sensitivity and cancer cell targeting, without the need for lengthy post-synthetic conjugation procedures, is expected to offer both time and cost savings over currently used methods in large-scale production. Furthermore, as the enhanced uptake of Arg is common amongst aggressive malignancies, the Arg/PAA-PSiNPs have potential to be used for *in vivo* drug delivery applications in a wide range of other cancer types.

CRediT authorship contribution statement

George Newham: Conceptualization, Methodology, Investigation, Formal analysis, Writing - original draft. **Ryan K. Mathew:** Resources, Writing - review & editing. **Heiko Wurdak:** Resources, Writing - review & editing. **Stephen D. Evans:** Supervision, Writing - review & editing. **Zhan Yuin Ong:** Conceptualization, Methodology, Supervision, Writing - review & editing, Funding acquisition.

Declaration of Competing Interest

None.

Acknowledgement

We gratefully acknowledge financial support from the University of Leeds and the EPSRC DTP studentship for G.N. (1950982). R.K.M. is funded by Yorkshire's Brain Tumour Charity and Candlelighters. S.D.E. acknowledges support from the Engineering and Physical Sciences Research Council (EP/P023266/1) and National Institute for Health Research infrastructure at Leeds. The raw experimental dataset obtained from this study is available to download from doi.org/10.5518/845.

Appendix A. Supplementary data

Supplementary data to this article can be found online at https://doi.org/10.1016/j.jcis.2020.10.133.

References

[1] I.I. Slowing, J.L. Vivero-Escoto, C.-W. Wu, V.S.Y. Lin, Mesoporous Silica Nanoparticles as Controlled Release Drug Delivery and Gene Transfection Carriers, Adv. Drug Deliv. Rev. 60 (11) (2008) 1278–1288.

[2] S. Chen, S.L. Greasley, Z.Y. Ong, P. Naruphontjirakul, S.J. Page, J.V. Hanna, A.N. Redpath, O. Tsigkou, S. Rankin, M.P. Ryan, A.E. Porter, J.R. Jones, Biodegradable Zinc-Containing Mesoporous Silica Nanoparticles for Cancer Therapy, Mater. Today Adv. 6 (2020) 100066.

[3] A.C. Anselmo, S. Mitragotri, Nanoparticles in the Clinic: An Update, Bioeng. Transl. Med. 4 (3) (2019) 1–16.

[4] S.-H. Wu, C.-Y. Mou, H.-P. Lin, Synthesis of Mesoporous Silica Nanoparticles, Chem. Soc. Rev. 42 (9) (2013) 3862.

[5] F. Lu, S.H. Wu, Y. Hung, C.Y. Mou, Size Effect on Cell Uptake in Well-Suspended, Uniform Mesoporous Silica Nanoparticles, Small 5 (12) (2009) 1408–1413.

[6] H.-P. Lin, C.-P. Tsai, Synthesis of Mesoporous Silica Nanoparticles from a Low-Concentration CnTMAX–Sodium Silicate Components, Chem. Lett. 32 (12) (2003) 1092–1093.

[7] C.E. Fowler, D. Khushalani, B. Lebeau, S. Mann, Nanoscale Materials with Mesostructured Interiors, Adv. Mater. 13 (9) (2001) 649–652.

[8] X. Lv, L. Zhang, F. Xing, H. Lin, Controlled Synthesis of Monodispersed Mesoporous Silica Nanoparticles: Particle Size Tuning and Formation Mechanism Investigation, Microporous Mesoporous Mater. 225 (2016) 238–244.

[9] R.R. Castillo, D. Lozano, B. González, M. Manzano, I. Izquierdo-Barba, M. Vallet-Regí, Advances in Mesoporous Silica Nanoparticles for Targeted Stimuli-Responsive Drug Delivery: An Update, Expert Opin. Drug Deliv. 16 (4) (2019) 415–439.

[10] C.C. Shiu, S. Wang, C.H. Chang, J.S. Jan, Poly(l -Glutamic Acid)-Decorated Hybrid Colloidal Particles from Complex Particle-Templated Silica Mineralization, J. Phys. Chem. B 117 (34) (2013) 10007–10016.

[11] J.J. Hu, Y.H. Hsieh, J.S. Jan, Polyelectrolyte Complex-Silica Hybrid Colloidal Particles Decorated with Different Polyelectrolytes, J. Colloid Interface Sci. 438 (2015) 94–101.

[12] V. Lauth, M. Maas, K. Rezwan, Coacervate-Directed Synthesis of CaCO3 Microcarriers for PH-Responsive Delivery of Biomolecules, J. Mater. Chem. B 2 (44) (2014) 7725–7731.

[13] H. Shi, L. Li, L. Zhang, T. Wang, C. Wang, D. Zhu, Z. Su, Designed Preparation of Polyacrylic Acid/Calcium Carbonate Nanoparticles with High Doxorubicin Payload for Liver Cancer Chemotherapy, CrystEngComm 17 (26) (2015) 4768–4773.

[14] H. Ren, L. Zhang, J. An, T. Wang, L. Li, X. Si, L. He, X. Wu, C. Wang, Z. Su, Polyacrylic Acid@zeolitic Imidazolate Framework-8 Nanoparticles with Ultrahigh Drug Loading Capability for PH-Sensitive Drug Release, Chem. Commun. 50 (8) (2014) 1000–1002.

[15] H. Ren, L. Zhang, T. Wang, L. Li, Z. Su, C. Wang, Universal and Facile Synthesis of Multicolored Upconversion Hollow Nanospheres Using Novel Poly(Acrylic Acid Sodium Salt) Microspheres as Templates, Chem. Commun. 49 (54) (2013) 6036–6038.

[16] Y. Wan, S.H. Yu, Polyelectrolyte Controlled Large-Scale Synthesis of Hollow Silica Spheres with Tunable Sizes and Wall Thicknesses, J. Phys. Chem. C 112 (10) (2008) 3641–3647.

[17] Y. Nakashima, C. Takai, C. Wanghui, H. Razavi-Khosroshahi, T. Shirai, M. Fuji, Control Size Distribution of Hollow Silica Nanoparticles by Viscosity of Emulsion Template, Colloids Surf. A Physicochem. Eng. Asp. 507 (2016) 164–169.

[18] Y. Nakashima, C. Takai, H. Razavi-Khosroshahi, M. Fuji, Influence of the PAA Concentration on PAA/NH3emulsion Template Method for Synthesizing Hollow Silica Nanoparticles, Colloids Surf. A Physicochem. Eng. Asp. 546 (2018) 301–306.

[19] C. Takai-Yamashita, M. Ando, M. Noritake, H.R. Khosroshahi, M. Fuji, Emulsion Templating of Poly (Acrylic Acid) by Ammonium Hydroxide/Sodium Hydroxide Aqueous Mixture for High-Dispersed Hollow Silica Nanoparticles, Adv. Powder Technol. 28 (2) (2017) 398–405.

[20] Y. Nakashima, C. Takai, H. Razavi-Khosroshahi, M. Fuji, Effects of Cations on the Size and Silica Shell Microstructure of Hollow Silica Nanoparticles Prepared Using PAA/Cation/NH4OH Template, Colloids Surfaces A Physicochem. Eng. Asp. 593 (February) (2020) 124582.

[21] N. Syed, J. Langer, K. Janczar, P. Singh, C. Lo Nigro, L. Lattanzio, H.M. Coley, E. Hatzimichael, J. Bomalaski, P. Szlosarek, M. Awad, K. O'Neil, F. Roncaroli, T. Crook, Epigenetic Status of Argininosuccinate Synthetase and Argininosuccinate Lyase Modulates Autophagy and Cell Death in Glioblastoma, Cell Death Dis. 4 (1) (2013) 1–11.

[22] C.M. Ensor, F.W. Holtsberg, J.S. Bomalaski, M.A. Clark, Pegylated Arginine Deiminase (ADI-SS PEG20,000 Mw) Inhibits Human Melanomas and Hepatocellular Carcinomas in Vitro and in Vivo, Cancer Res. 62 (19) (2002) 5443–5450.

[23] R.H. Kim, J.M. Coates, T.L. Bowles, G.P. McNerney, J. Sutcliffe, J.U. Jung, R. Gandour-Edwards, F.Y.S. Chuang, R.J. Bold, H.J. Kung, Arginine Deiminase as a Novel Therapy for Prostate Cancer Induces Autophagy and Caspase-Independent Apoptosis, Cancer Res. 69 (2) (2009) 700–708.

[24] Y. Lu, W. Wang, J. Wang, C. Yang, H. Mao, X. Fu, Y. Wu, J. Cai, J. Han, Z. Xu, Z. Zhuang, Z. Liu, H. Hu, B. Chen, Overexpression of Arginine Transporter CAT-1 Is Associated with Accumulation of L-Arginine and Cell Growth in Human Colorectal Cancer Tissue, PLoS One 8 (9) (2013) 1–8.

[25] S. Wang, F. Li, R. Qiao, X. Hu, H. Liao, L. Chen, J. Wu, H. Wu, M. Zhao, J. Liu, R. Chen, X. Ma, D. Kim, J. Sun, T.P. Davis, C. Chen, J. Tian, T. Hyeon, D. Ling, Arginine-Rich Manganese Silicate Nanobubbles as a Ferroptosis-Inducing Agent for Tumor-Targeted Theranostics, ACS Nano 12 (12) (2018) 12380–12392.

[26] J. Rouquerol, P. Llewellyn, F. Rouquerol, Is the BET Equation Applicable to Microporous Adsorbents?, Elsevier B.V. 160 (2007).

[27] R.W. Korsmeyer, R. Gurny, E. Doelker, P. Buri, N.A. Peppas, Mechanisms of Solute Release from Porous Hydrophilic Polymers, Int. J. Pharm. 15 (1) (1983) 25–35.

[28] E.S. Polson, V.B. Kuchler, C. Abbosh, E.M. Ross, R.K. Mathew, H.A. Beard, B. Da Silva, A.N. Holding, S. Ballereau, E. Chuntharpursat-Bon, J. Williams, H.B. Griffiths, H. Shao, A. Patel, A.J. Davies, A. Droop, P. Chumas, S.C. Short, M. Lorger, J.E. Gestwicki, L.D. Roberts, R.S. Bon, S.J. Allison, S. Zhu, F. Markowetz, H. Wurdak, KHS101 Disrupts Energy Metabolism in Human Glioblastoma Cells and Reduces Tumor Growth in Mice. Sci. Transl. Med. 2018, 10 (454).

[29] H. Wurdak; S. Zhu, A. Romero, M. Lorger, J. Watson, C. yuan Chiang, J. Zhang, V. S. Natu, L.L. Lairson, J.R. Walker, C.M. Trussell, G.R. Harsh, H. Vogel, B. Felding-Habermann, A.P. Orth, L.J. Miraglia, D.R. Rines, S.L. Skirboll, P.G. Schultz, An RNAi Screen Identifies TRRAP as a Regulator of Brain Tumor-Initiating Cell Differentiation. Cell Stem Cell 2010, 6 (1), 37–47.

[30] Z. Teng, Y. Han, J. Li, F. Yan, W. Yang, Preparation of Hollow Mesoporous Silica Spheres by a Sol-Gel/Emulsion Approach, Microporous Mesoporous Mater. 127 (1–2) (2010) 67–72.

[31] J. Xu, X. Li, J. Li, X. Li, B. Li, Y. Wang, L. Wu, W. Li, Wet and Functional Adhesives from One-Step Aqueous Self-Assembly of Natural Amino Acids and Polyoxometalates, Angew. Chemie - Int. Ed. 56 (30) (2017) 8731–8735.

[32] X. Liu, X. Xie, Z. Du, B. Li, L. Wu, W. Li, Aqueous Self-Assembly of Arginine and K8SiW11O39: Fine-Tuning the Formation of a Coacervate Intended for Sprayable Anticorrosive Coatings, Soft Matter 15 (45) (2019) 9178–9186.

[33] J.-G. Park, S.-H. Lee, J.-S. Ryu, Y.-K. Hong, T.-G. Kim, A.A. Busnaina, Interfacial and Electrokinetic Characterization of IPA Solutions Related to Semiconductor Wafer Drying and Cleaning, J. Electrochem. Soc. 153 (9) (2006) G811.

[34] A. Gupta, H.B. Bohidar, Kinetics of Phase Separation in Systems Exhibiting Simple Coacervation, Phys. Rev. E - Stat. Nonlinear, Soft Matter Phys. 72 (1) (2005) 1–9.

[35] J.T.G. Overbeek, M.J. Voorn, Phase Separation in Polyelectrolyte Solutions. Theory of Complex Coacervation, J. Cell. Comp. Physiol. 49 (S1) (1957) 7–26.

[36] G. Zhang, C. Wu, Reentrant Coil-to-Globule-to-Coil Transition of a Single Linear Homopolymer Chain in a Water/Methanol Mixture, Phys. Rev. Lett. 86 (5) (2001) 822–825.

[37] G. Åkerlöf, Dielectric Constants of Some Organic Solvent-Water Mixtures at Various Temperatures, J. Am. Chem. Soc. 54 (11) (1932) 4125–4139.

[38] T. Swift, L. Swanson, M. Geoghegan, S. Rimmer, The PH-Responsive Behaviour of Poly(Acrylic Acid) in Aqueous Solution Is Dependent on Molar Mass, Soft Matter 12 (9) (2016) 2542–2549.

[39] C. Brinker, Hydrolysis and Condensation of Silicates: Effects on Structure, J. Non-Cryst. Solids 100 (1988) 31–50.

[40] D.R. Lide, Ed. CRC Handbook of Chemistry and Physics, Internet V.; CRC Press: Boca Ranton, FL, 2005; Vol. Internet V.

[41] H. Li, H. Yu, C. Zhu, J. Hu, M. Du, F. Zhang, D. Yang, Cisplatin and Doxorubicin Dual-Loaded Mesoporous Silica Nanoparticles for Controlled Drug Delivery, RSC Adv. 6 (96) (2016) 94160–94169.

[42] T. Yokoi, J. Wakabayashi, Y. Otsuka, W. Fan, M. Iwama, R. Watanabe, K. Aramaki, A. Shimojima, T. Tatsumi, T. Okubo, Mechanism of Formation of Uniform-Sized Silica Nanospheres Catalyzed by Basic Amino Acids, Chem. Mater. 21 (15) (2009) 3719–3729.

[43] X. Du, J. He, Carrier Effect in the Synthesis of Rattle-Type Au@hollow Silica Nanospheres by Impregnation and Thermal Decomposition Method, Microporous Mesoporous Mater. 163 (2012) 201–210.

[44] E. Roy, S. Patra, R. Madhuri, P.K. Sharma, Development of an Imprinted Polymeric Sensor with Dual Sensing Property for Trace Level Estimation of Zinc and Arginine, Mater. Sci. Eng. C 49 (2015) 25–33.

[45] W. Kam, C.W. Liew, J.Y. Lim, S. Ramesh, Electrical, Structural, and Thermal Studies of Antimony Trioxide-Doped Poly(Acrylic Acid)-Based Composite Polymer Electrolytes, Ionics (Kiel). 20 (5) (2014) 665–674.

[46] J. Yan, X. Xu, J. Zhou, C. Liu, L. Zhang, D. Wang, F. Yang, H. Zhang, Fabrication of a PH/Redox-Triggered Mesoporous Silica-Based Nanoparticle with Microfluidics for Anticancer Drugs Doxorubicin and Paclitaxel Codelivery, ACS Appl. Bio Mater. 3 (2) (2020) 1216–1225.

[47] J. Li, S. Shen, F. Kong, T. Jiang, C. Tang, C. Yin, Effects of Pore Size on. In Vitro and in Vivo Anticancer Efficacies of Mesoporous Silica Nanoparticles, RSC Adv. 8 (43) (2018) 24633–24640.

[48] M. Xie, H. Shi, Z. Li, H. Shen, K. Ma, B. Li, S. Shen, Y. Jin, A Multifunctional Mesoporous Silica Nanocomposite for Targeted Delivery, Controlled Release of Doxorubicin and Bioimaging, Colloids Surf. B Biointerfaces 110 (2013) 138–147.

[49] J. Yue, Luo, S. zhong, Lu, M. meng, Shao, D. Wang, Z. Dong, W. fei, A Comparison of Mesoporous Silica Nanoparticles and Mesoporous Organosilica Nanoparticles as Drug Vehicles for Cancer Therapy. Chem. Biol. Drug Des. 2018, 92 (2), 1435–1444.

[50] J. Shen, Q. He, Y. Gao, J. Shi, Y. Li, Mesoporous Silica Nanoparticles Loading Doxorubicin Reverse Multidrug Resistance: Performance and Mechanism, Nanoscale 3 (10) (2011) 4314–4322.

[51] L. Yuan, Q. Tang, D. Yang, J.Z. Zhang, F. Zhang, J. Hu, Preparation of PH-Responsive Mesoporous Silica Nanoparticles and Their Application in Controlled Drug Delivery, J. Phys. Chem. C 115 (20) (2011) 9926–9932.

[52] B. Tian, S. Liu, S. Wu, W. Lu, D. Wang, L. Jin, B. Hu, K. Li, Z. Wang, Z. Quan, PH-Responsive Poly (Acrylic Acid)-Gated Mesoporous Silica and Its Application in Oral Colon Targeted Drug Delivery for Doxorubicin, Colloids Surfaces B Biointerfaces 154 (2017) 287–296.

[53] P. Bilalis, L.A. Tziveleka, S. Varlas, H. Iatrou, PH-Sensitive Nanogates Based on Poly(l-Histidine) for Controlled Drug Release from Mesoporous Silica Nanoparticles, Polym. Chem. 7 (7) (2016) 1475–1485.

[54] K. Leung, I.M.B. Nielsen, L.J. Criscenti, Elucidating the Bimodal Acid-Base Behavior of the Water-Silica Interface from First Principles, J. Am. Chem. Soc. 131 (51) (2009) 18358–18365.